

**Combined thermodynamic-kinetic-competitive controls on anaerobic respiration pathways and the chemistry of natural waters**

Sergei Katsev<sup>a,1,2</sup> and Itay Halevy<sup>b,1,2</sup>

<sup>a</sup> Large Lakes Observatory, University of Minnesota Duluth, Duluth, MN 55812, USA

<sup>b</sup> Earth and Planetary Sciences, Weizmann Institute of Science, Rehovot 76100, Israel

<sup>1</sup> Equal contribution.

<sup>2</sup> Correspondence: [skatsev@d.umn.edu](mailto:skatsev@d.umn.edu), [itay.halevy@weizmann.ac.il](mailto:itay.halevy@weizmann.ac.il)

This is a non-peer-reviewed preprint submitted to EarthArXiv.

---

Please note the manuscript has yet to be formally accepted for publication. Subsequent versions of this manuscript may have slightly different content. If accepted, the final version of this manuscript will be available via the 'Peer-reviewed Publication DOI' link on the right-hand side of this webpage. Please feel free to contact any of the authors; we welcome feedback.

---

# Combined thermodynamic-kinetic-competitive controls on anaerobic respiration pathways and the chemistry of natural waters

Sergei Katsev <sup>a,1,2</sup> Itay Halevy <sup>b,1,2</sup>

<sup>a</sup>Large Lakes Observatory, University of Minnesota Duluth, Duluth, MN 55812, USA

<sup>b</sup>Earth and Planetary Sciences, Weizmann Institute of Science, Rehovot 76100, Israel

<sup>1</sup>Equal contribution.

<sup>2</sup>Correspondence: skatsev@d.umn.edu, itay.halevy@weizmann.ac.il.

## ABSTRACT

1 **Microbial metabolisms underpin geochemical cycling in nearly all of the Earth's biosphere. Anaerobic pathways of carbon**  
2 **mineralization by iron and sulfate reduction and methanogenesis, in particular, have existed over most of Earth history and**  
3 **have been central in shaping the chemistry of the oceans and atmosphere. The governing principles by which microbial**  
4 **metabolisms contribute to water-column chemistry, however, are incompletely understood in natural systems where mi-**  
5 **crobes compete for resources. Contrary to common assumptions, thermodynamics often fails to reproduce the observed**  
6 **metabolic succession. Here, we analyze the coupled effects of thermodynamics, kinetics, population dynamics, and phys-**  
7 **ical transport on the composition of microbial communities, their integrated rates of metabolic activity, and effects on the**  
8 **chemistry of aqueous environments. Together, these controls explain the microbiology and chemistry of modern lakes and**  
9 **seas, and constrain the expected variability in the Earth's oceans over geologic time. We find, in particular, that microbial**  
10 **sulfate reduction, despite being less thermodynamically favored than iron reduction, can account for a significant fraction**  
11 **of organic matter remineralization, even without producing measurable concentrations of aqueous sulfide. In ferruginous**  
12 **water columns, methanogenesis is viable under low ( $<\sim 100 \mu\text{M}$ ) sulfate conditions, but methane accumulation in early**  
13 **oceans was unlikely before a widespread oxygenation of the ocean surface. We also illustrate how processes in anoxic wa-**  
14 **ter columns become reflected in the deposition of iron sulfide minerals that are commonly used as proxies of paleoredox**  
15 **conditions.**

## 16 SIGNIFICANCE STATEMENT

17 Biogeochemical reactions in anoxic sediments and water columns are traditionally assumed to proceed in a sequence determined  
18 by the thermodynamics of the respective microbial metabolic pathways, with multiple exceptions being explained ad-hoc. Here,  
19 we develop a theoretical framework that accounts for the competitive growths of microbial populations and their known physio-  
20 logical capabilities. We show that competition among microbial populations, together with local physical transport, are essential for  
21 defining geochemical outcomes. The developed theoretical approach explains several previously enigmatic observations, outlines  
22 ecological niches for microbial populations, creates a framework for interpreting marine chemistry on Early Earth, and may help un-  
23 derstand the drivers for the evolution of microbial capabilities.

## 24 INTRODUCTION

25 Where oxygen is unavailable, organic matter is mineralized by competing anaerobic pathways, catalyzed by diverse microbial pop-  
26 ulations. Perhaps most consequential for ocean chemistry is the split of anaerobic mineralization of organic carbon among dis-  
27 similatory sulfate reducers, iron reducers, and methanogens. Over the course of the Earth's geologic history, this split controlled  
28 the chemical composition of the ocean interior, fluxes of toxic hydrogen sulfide to the surface biosphere, and fluxes of methane to  
29 the atmosphere<sup>1,2</sup>. The partitioning among these metabolisms is usually considered to reflect their thermodynamic favorability  
30 and/or the relative supply rates of sulfur, iron, and carbon. Observations, however, diverge from this simple view<sup>3</sup>. Methanogenesis  
31 is known to be highly viable in the presence of reactive iron oxides<sup>4,5</sup>, and sulfate reduction often outpaces iron reduction<sup>3</sup>. Like-  
32 wise, in sediments<sup>6</sup> and in ferruginous water columns<sup>7</sup> of low-sulfate lakes, a substantial fraction of reactive iron is reduced abioti-  
33 cally by the sulfide produced during sulfate reduction, rather than by microbial iron reduction. These deviations from the canonical  
34 thermodynamic sequence have sometimes been explained by the dependence of iron reduction energetics on solution pH and

35 the mineralogy and crystallinity of iron oxides<sup>3</sup>. In other cases, such deviations have been attributed to challenges faced by some  
36 microbial communities, such as for iron reducers to gain access to solid mineral surfaces<sup>8</sup>. Rates of microbially-catalyzed geochem-  
37 ical reactions, however, also depend on cell populations, which are affected by conditions for microbial growth, competition for sub-  
38 strates, and population dynamics in a physically changing environment. Effects of these additional factors have not been systemati-  
39 cally explored, confounding the interpretations of many aspects of aqueous biogeochemistry in modern and ancient environments.  
40 For much of Earth history, reduced products ( $\text{H}_2\text{S}$ ,  $\text{Fe}^{2+}$  and  $\text{CH}_4$ ) of anaerobic metabolisms could accumulate in deep ocean wa-  
41 ters, depending on their relative rates of production and consumption. Precipitation of insoluble iron sulfide minerals could remove  
42 the element (either sulfur or iron) that was supplied at a lower rate, allowing the other to accumulate. Whether the deep waters be-  
43 came ferruginous (iron-rich) or euxinic (sulfide-rich) had far-reaching implications for biogeochemical cycles and the biosphere.  
44 Sedimentary rock records, mostly of iron speciation, have been interpreted to infer predominantly ferruginous marine conditions  
45 during the Archean and Proterozoic eons, with notable occurrences of euxinia limited in either space or time<sup>9</sup>. Global climate is  
46 strongly affected by rates of marine methanogenesis and the methane fluxes to the atmosphere, which are in turn strongly atten-  
47 uated by sulfate via microbially-catalyzed oxidation<sup>10</sup>. Understanding the evolution of the ocean-atmosphere system, therefore, re-  
48 quires understanding of the controls on the drawdown of seawater sulfate and the development of ferruginous versus euxinic con-  
49 ditions.

50 In addition to chemical processes, physical transport must also be important. For example, the zone of iron reduction in sediments  
51 is typically situated near the oxic-anoxic boundary and above the zone of sulfate reduction, in accordance with the thermodynamic  
52 favorability of iron reduction. In water columns, in contrast, mid-water euxinia is a well-recognized phenomenon in ferruginous wa-  
53 ter bodies<sup>11</sup>. A mid-water ferruginous layer in an otherwise euxinic water column has not been observed, to our knowledge, de-  
54 spite the thermodynamic favorability of iron reduction. The rates of physical transport, especially in relation to the rates of (bio)chemical  
55 reactions that produce or consume the involved substrates, thus strongly influence the patterns of dominant chemical species and  
56 microbial populations.

57 Physico-chemical dynamics in chemically stratified aquatic environments have been successfully explored in the past using reaction-  
58 transport models<sup>12,13</sup>, some of which explicitly considered the dynamics of microbial biomass<sup>14,15</sup>. Such models have more re-  
59 cently begun to incorporate genomic, transcriptomic and proteomic data<sup>16,17</sup>. For specific environments with well characterized  
60 conditions, biogeochemical kinetics may be parameterized from observations or sometimes calculated theoretically<sup>13,18</sup>. For a  
61 wider spectrum of environments, however, one needs to account for the growth rates of microbial populations<sup>19</sup>, each with their  
62 own (and varying) cell-specific rates of reactions that they catalyze. One way to couple the rates of chemical reactions and biomass  
63 growth is through the energetics of microbial metabolisms<sup>20,21</sup>. Biomass growth depends on the balance between the energy fur-  
64 nished to cells by their catabolic reactions and the energy required for their anabolism. The energetics-based approach, while re-  
65 lying on experimental data for microbial kinetics, allows accounting for the relative differences in the growth rates among popula-  
66 tions, when they compete for substrates in the same environment. Studies without a spatial component<sup>18,22,23</sup> used this approach  
67 to successfully simulate the patterns of microbial populations and their metabolic pathways under a range of conditions. The use  
68 of such models<sup>19,24</sup> in dynamic water columns, where both cells and their substrates are physically transported (often at disparate  
69 rates) across concentration gradients, has been so far unexplored.

70 Here, we incorporate such competitive microbial dynamics into a reactive-transport model, and explore the patterns of geomicrobi-  
71 ological activity that result in redox-stratified water columns under a wide range of conditions. We analyze how such patterns corre-  
72 spond to observations in modern marine and freshwater environments, and explore their likely manifestations in ocean chemistry  
73 of the geologic past.

## 74 **CONTROLS ON ANAEROBIC RESPIRATION PATHWAYS**

75 The rates of microbially-catalyzed dissimilatory iron reduction (IR), sulfate reduction (SR), and methanogenesis (MG) are determined  
76 by the combined influences of thermodynamic, kinetic, physiological, and population dynamics factors. These factors have compet-  
77 ing effects, manifested differently in different environments, and it is instructive to analyze them individually.

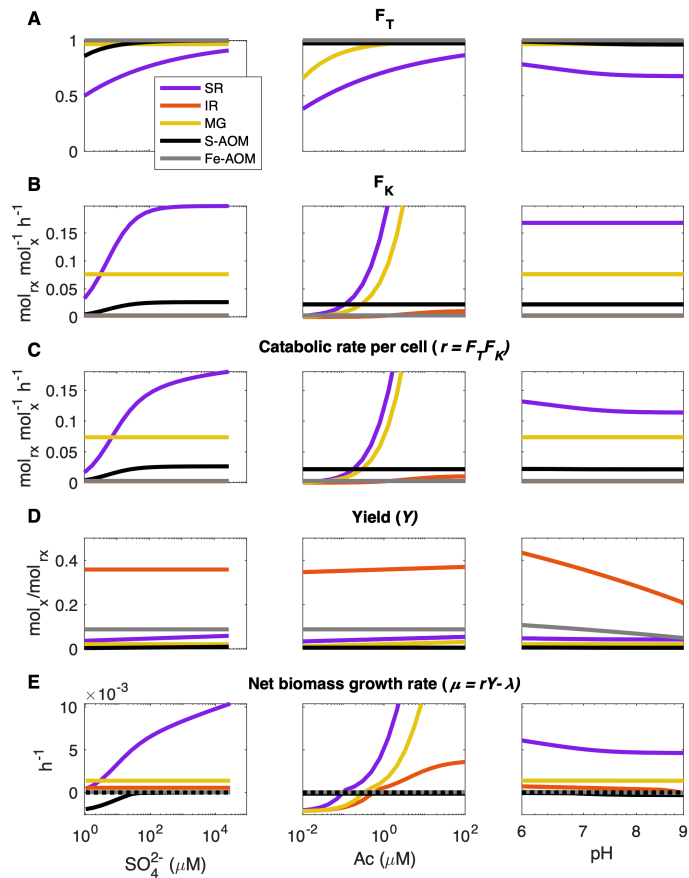


**Figure 1:** Thermodynamic and kinetic characteristics of selected anaerobic microbial pathways, as functions of the concentrations of sulfate, acetate (as electron donor), and the pH. A) Thermodynamic limitation factor  $F_T$ ; B) Kinetic limitation factor  $F_K$ ; C) Rate of catabolic reaction per C-mol of cell biomass; D) Energetics-based biomass yield  $Y$  in C-mol of biomass created per mol of catabolic reaction; E) Net (growth minus death) rate of biomass growth  $\mu$ . Values of the (non-varied) parameters:  $[\text{SO}_4^{2-}] = 28 \mu\text{M}$ ,  $[\text{Ac}] = 1 \mu\text{M}$ ,  $\text{pH} = 7$ ,  $[\text{Fe}^{2+}] = 1 \mu\text{M}$ ,  $[\text{CH}_4] = 10 \mu\text{M}$ ,  $[\text{H}_2\text{S}] = 10 \mu\text{M}$ ,  $T = 4^\circ\text{C}$ , and goethite as the Fe(III) solid phase  $[\text{FeOOH}] = 111 \mu\text{mol/L}$ . Kinetic parameters are listed in Table 1. Different conditions can result in different relative favorabilities of the illustrated pathways.

## 78 Thermodynamics

79 The canonical view is that iron reduction is more energetically favorable than sulfate reduction, which is in turn more favorable than  
 80 methanogenesis. The pH and the mineralogy and crystallinity of ferric iron particles, however, have been shown to affect the ther-  
 81 modynamic drive for iron reduction, creating differences in the order of favorability of anaerobic respiration reactions<sup>3,25</sup>. Neverthe-  
 82 less, oxidation of acetate with goethite generates nearly 400 kJ/mol at typical environmental conditions, while acetoclastic sulfate  
 83 reduction and methanogenesis provide an order of magnitude less energy (the difference being smaller at higher pH; Fig. 1). Far  
 84 from thermodynamic equilibrium, biochemical reaction rates are determined by kinetic, rather than energetic, factors. Thermody-  
 85 namic limitation, however, becomes important when the energy obtained by the microorganism per reaction turnover becomes  
 86 comparable to the energy that may be conserved as ATP. The corresponding effect on bioreaction kinetics is commonly described  
 87 with a dimensionless thermodynamic factor  $F_T$ , between 0 and 1, which reflects the catabolic free energy available after ATP syn-  
 88 thesis (Methods Eq. 5; Fig. 1A). Since the number of ATP molecules synthesized per reaction turnover varies among metabolic path-  
 89 ways<sup>3</sup>, the effect of energy availability on  $F_T$  also varies. Methanogenic archaea, for example, while having less available catabolic  
 90 energy from the environment (less negative  $\Delta G_{cat}$ ) than sulfate reducers, synthesize fewer ATP molecules per reaction turnover<sup>3</sup>.  
 91 This can leave methanogens with more energy than sulfate reducers for the combined biochemical reaction, providing a greater  
 92 thermodynamic drive (higher  $F_T$ , Fig. 1A).

## 93 Kinetics

94 Microbes with different metabolisms face different challenges. Whereas sulfate reducers obtain their substrates from bulk solution,  
 95 iron-reducer activity is limited to surfaces of Fe(III) particles. At the cell level, kinetics of biogeochemical reactions are affected by the

96 physiological capabilities related to the inventory, structure and dynamics of enzymes and the transfer of metabolites in and out of  
97 the cell. These pathway-dependent differences are commonly described using pathway-specific kinetic factors ( $F_K$ , Methods Eq. 4;  
98 Fig. 1B), which express Monod-type dependencies on substrate concentrations using a maximum cell-specific rate  $V_{max}$  and a half-  
99 maximum concentration  $K_m$  that reflects the affinity towards a given substrate. Experimental data suggest that sulfate reducers  
100 and methanogens can metabolize their electron donor substrates approximately one to two orders of magnitude faster (on a per-  
101 cell basis,  $V_{max}$ ) than iron reducers<sup>26,27</sup> (Table 1). Sulfate and iron reducers, however, can access organic substrates such as acetate  
102 (and likely also  $H_2$ ;<sup>28</sup>) at lower concentrations (lower  $K_m$  towards acetate) than methanogens (Table 1;<sup>29,30</sup>).

### 103 Cell-specific rates

104 Taken together, thermodynamic and kinetic factors predict higher rates of cell-specific acetate oxidation by sulfate reducers than  
105 by iron reducers (Fig. 1C), under a wide range of environmentally relevant conditions. Methanogens are also predicted to consume  
106 acetate faster than iron reducers, although this changes at higher concentrations of reactive Fe(III), such as in sediments. At low sul-  
107 fate concentrations ( $< \sim 10 \mu M$ ) and methane concentrations on the order of  $10 \mu M$  (Fig. 1C), methanogens are additionally pre-  
108 dicted to have higher cell-specific catabolic rates than sulfate reducers. These predictions are based solely on the characteristics of  
109 individual catabolisms and account for neither the efficiency of anabolisms nor the outcome of competition among the different  
110 metabolic groups. Rate favorabilities could be different for different electron donors, such as  $H_2$  or for small organic molecules other  
111 than acetate (e.g., lactate).

### 112 Biosynthesis

113 The higher energy yield ( $\Delta G_r$ ) of IR means that iron reducers are expected to produce more biomass per mole of organic carbon  
114 oxidized (Fig. 1D). Their lower cell-specific catabolic rates, however, mean that this energetic advantage does not necessarily trans-  
115 late into a faster biomass growth. To compare growth rates ( $\mu$ ) among different metabolic groups, one needs to compare prod-  
116 ucts ( $rY$ ) of the thermodynamics-based yields  $Y$  of biomass per reaction turnover and the respective reaction rates  $r$ . For exam-  
117 ple, the biomass yield  $Y$  of iron reducers is about 7.5 times greater than for sulfate reducers (Fig. 1D), but their cell-specific catabolic  
118 rate capacity  $V_{max}$  is 10-100 times lower<sup>27,31</sup>. Thus, at sulfate concentrations exceeding several micromolar, the population of sul-  
119 fate reducers would grow faster than the population of iron reducers (Fig. 1E), and the bulk rate of sulfate reduction could be corre-  
120 spondingly greater. Similarly, high cell-specific rates of methanogenesis may sustain high rates of bulk reaction, despite the low en-  
121 ergy yield per electron donor and a low biomass growth rate. Differences in biomass yield and cell-specific catabolic rates between  
122 metabolic groups are expected to vary with substrate and product concentrations, temperature and the pH. Under certain combi-  
123 nations of these parameters, a microbial population dominated by iron-reducer biomass may, for example, display higher bulk rates  
124 of sulfate reduction than iron reduction. We note that the variation of kinetic parameters with the environmental parameters is cur-  
125 rently poorly constrained.

126 Importantly, for slow-growing populations, rates of microbial death (from energy starvation, viral lysis, etc.) may impose an addi-  
127 tional limit, as growth rates must not fall below death rates. The calculations in Fig. 1E, for example, suggest that sulfate-driven AOM,  
128 while thermodynamically favorable, may become prohibitively slow at low methane concentrations and sulfate concentrations be-  
129 low  $100 \mu M$ , which may explain the absence of sulfate-driven AOM observations in freshwater. The model similarly predicts stunted  
130 growth of sulfate reducers and methanogens at sub-micromolar concentrations of acetate, consistent with observations of micromolar-  
131 level residual acetate concentrations in sulfate-reducing and methanogenic zones of marine and freshwater sediments<sup>32-34</sup>.

### 132 Population Dynamics

133 Cell abundances in natural environments are strongly affected by interactions with other microbial populations. As concentrations  
134 of growth-limiting substrates are dynamically adjusted by competition or mutualism, conditions may become variably favorable  
135 for one type of metabolic group or another. Growth conditions can be also affected by toxicity. Slow-growing populations may be  
136 further disadvantaged by physical flows, as metabolizing cells may exit the system before they can divide. This complicates predic-  
137 tions of pathway dominance that are based on thermodynamics, kinetics, or biomass yields alone<sup>3</sup>. Figure 2 illustrates the simu-  
138 lated outcomes of the combined growth of iron-reducing, sulfate-reducing, and methanogenic microbes in a spatially homoge-

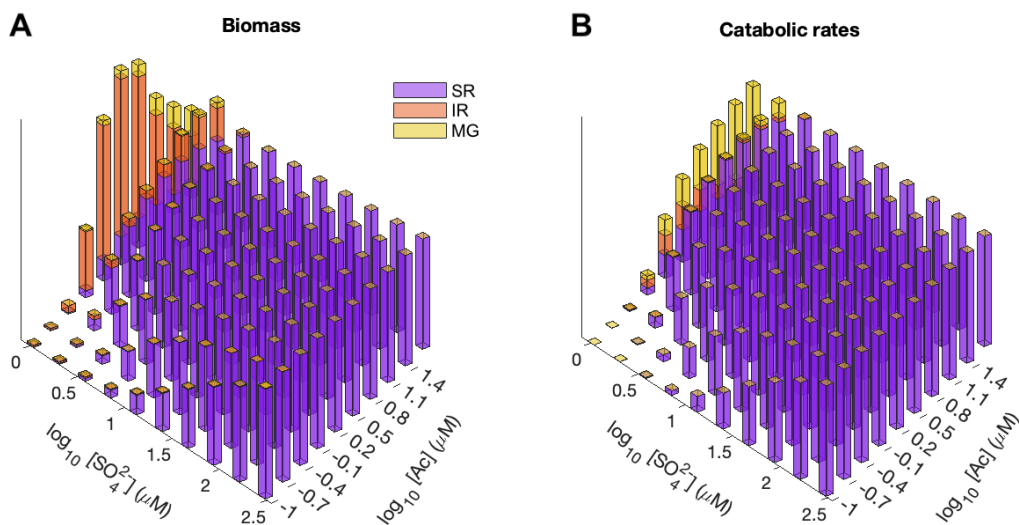


**Figure 2:** Microbial biomasses (A) and catabolic rates (B) in a simulated flow-through reactor at a steady state, as a function of electron donor (acetate) and sulfate concentrations. Sulfate reducers dominate when sulfate exceeds  $\mu\text{M}$  levels. High biomasses of iron reducers do not necessarily translate into high catabolic rates of acetate consumption. Competition results depend on the ratio of  $K_m$  values for the affinities for acetate for the involved populations. At low ratios of the iron-reducer to sulfate-reducer  $K_m$  (e.g., 1:4), a high affinity for acetate gives iron reducers an advantage at low acetate concentrations. At higher ratios (e.g., 1:1), iron reducers can be outcompeted by methanogens or sulfate reducers. For better visibility, biomasses and rates were normalized to their respective values for the maximum sulfate level at each of the acetate concentrations.

139 neous flow-through reactor. Despite the higher biomass yield of iron reducers, the higher cell-specific catabolic rates of sulfate re-  
 140 ducers and methanogens allow them to be the dominant consumers of acetate. At micromolar sulfate concentrations, most of the  
 141 organic carbon is mineralized through methanogenesis. At sulfate concentrations above several tens of  $\mu\text{M}$ , sulfate reducers dom-  
 142 inate both the biomass pools and carbon mineralization, in agreement with observations<sup>29</sup>. Iron reducers, nevertheless, may con-  
 143 stitute a significant portion of the microbial biomass under some conditions, as their high catabolic energy allows them to harvest  
 144 a proportionally greater fraction of the total energy. Iron reducers may also gain an advantage if they are able to access acetate at  
 145 significantly lower levels than their competitors, a possibility that is hinted at by some data<sup>30</sup> but is still poorly constrained.

#### 146 Physical transport

147 In natural aquatic environments, advection, turbulence, and molecular diffusion transport the reactive substrates and products, as  
 148 well as living cells themselves, to and from reaction zones, controlling metabolic rates and cell abundances. Effects of these phys-  
 149 ical processes are different for different respiratory pathways and may influence the outcomes of competition among metabolic  
 150 groups.

151 In chemically stratified water bodies, sulfate is supplied across the chemocline by processes such as turbulent diffusion, whose rates  
 152 increase with the concentration gradient. Fluxes of solid iron oxides, in contrast, are determined primarily by settling of particles.  
 153 This means that, while sulfate reducers can access more sulfate by increasing their metabolic rate of sulfate consumption, thereby  
 154 increasing the concentration gradient, iron reducers lack such an opportunity for positive feedback. This gives sulfate reducers an  
 155 additional local advantage. On a global scale, over timescales comparable to the residence time of seawater sulfate, the feedback is  
 156 likely weakened if high rates of sulfate reduction decrease the size of the oceanic sulfate pool.

157 To a similar effect, most reactive iron oxyhydroxide phases are nanosize particles, which settle through the water column much slower  
 158 than more crystalline, coarser-grained iron oxides. Produced at the redoxcline via oxidation of the upwardly diffusing or upwelling  
 159  $\text{Fe}^{2+}$ , the nanosize and highly reactive Fe(III) particles can be consumed immediately below the redoxcline by reaction with hydro-  
 160 gen sulfide. Such sulfide scavenging maintains a thermodynamic drive for sulfate reduction and decreases Fe(III) oxide availability  
 161 for microbial iron reduction, further increasing the advantage of sulfate reducers.

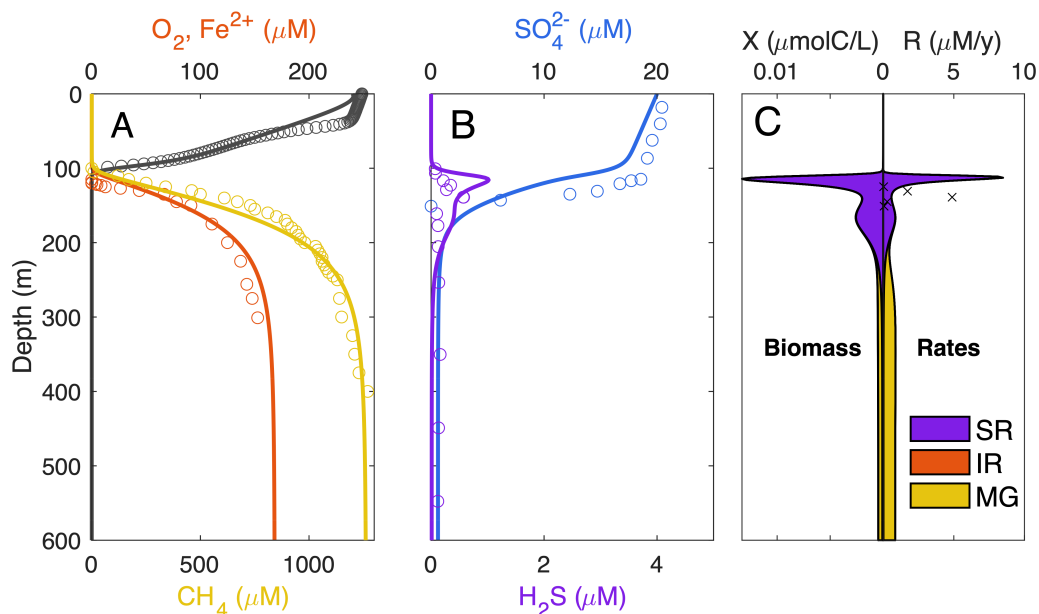


**Figure 3:** Profiles of water-column chemistry (A, B) and anaerobic microbe biomasses and respiration rates (C) simulated for the meromictic ferruginous Lake Matano. Circles represent measured concentrations, whereas black 'x' are measured sulfate reduction rates<sup>35,36</sup>. Vertical mixing rates were approximated after<sup>37</sup>.

## 162 BIOGEOCHEMISTRY OF STRATIFIED WATER COLUMNS

163 In spatially extended systems, the above processes shape biogeochemical zonations: partitioning of organic matter respiration among  
 164 metabolisms, variations in microbial cell densities and metabolic rates, and the resultant aqueous chemistry. To elucidate the pat-  
 165 terns of such zonations in stratified water columns, we combined the above thermodynamic, kinetic, and competitive controls in a  
 166 biomass-explicit reaction-transport model (see Materials and Methods). For a reasonable set of parameters (see SI), for example, the  
 167 model reproduces the water-column chemistry and microbial respiration rates observed in ferruginous Lake Matano (Fig. 3). We  
 168 then used the model to explore the likely biogeochemical scenarios under a wide range of anoxic environmental conditions, such  
 169 as those that existed in marine coastal waters during the Archean and Proterozoic eons, and those that are found today in restricted  
 170 marine basins and meromictic freshwater lakes.

171 Contrary to the thermodynamic sequence, we find that sulfate reducers commonly dominate both the microbial biomass and bulk  
 172 geochemical rates in anoxic waters (Figs. 4, S1, S2). This dominance arises from the favorable kinetics of sulfate reduction (Fig. 1), a  
 173 positive feedback between the steepness of the sulfate concentration gradient and the rate of bulk sulfate reduction, and the scav-  
 174 enging of Fe(III) oxyhydroxide particles by sulfide. The water-column chemistry does not always reflect the dominant metabolism  
 175 (Figs. 3, 4). Deep waters dominated by sulfate reducers (or methanogens) may remain ferruginous, while sulfide may not build up  
 176 because of its scavenging by upwelled iron (Fig. 4). The reverse situation—a euxinic water column dominated by iron reducers—is  
 177 unlikely to occur because of the lack of Fe(III) substrates: Abiotic sulfidization of the Fe(III) oxyhydroxides settling from the ocean sur-  
 178 face strongly competes with microbial iron reduction (Fig. S1), whereas euxinic water lacks Fe<sup>2+</sup> that could be oxidized to produce  
 179 Fe(III) near the redoxcline.

180 As our simulations illustrate, in the absence of strong external sources of iron, robust ferruginous conditions are unlikely to develop  
 181 when surface sulfate concentrations exceed  $\sim 100 \mu\text{M}$ . Modern low-sulfate systems conform to this pattern: nearly all known fer-  
 182 ruginous lakes<sup>11</sup> have sulfate concentrations below  $100 \mu\text{M}$ , whereas water bodies with higher sulfate levels are sulfidic. For anoxic  
 183 columns with ferruginous deep waters, simulations predict at least some mid-water euxinia (Fig. 4), again a common pattern in  
 184 modern lakes<sup>38,39</sup> and a widely hypothesized scenario for ancient oceans. Concentrations of dissolved Fe<sup>2+</sup> in excess of  $\sim 10$ s of  $\mu\text{M}$   
 185 generally cannot be sustained by water-column iron reduction, and require an upward flux of Fe<sup>2+</sup> from below. In ferruginous lakes  
 186 such fluxes usually come from sediments (Fig. 3). In the ancient ferruginous oceans, Fe<sup>2+</sup> was likely supplied by upwelling from the  
 187 deep ocean, where it came from hydrothermal inputs and the reduction of sinking particles.

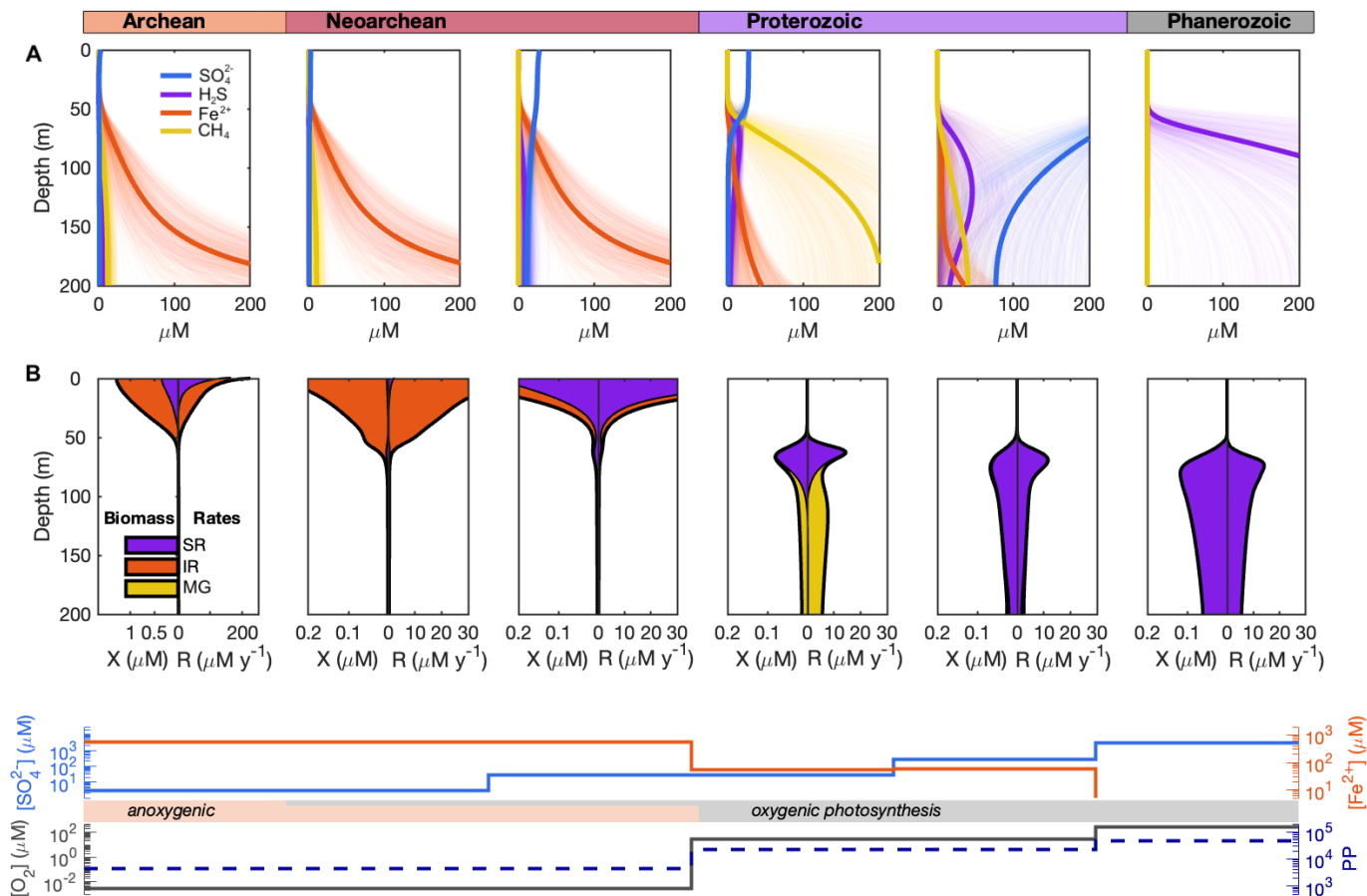


**Figure 4:** Average profiles of water-column chemistry (A) and anaerobic microbial biomasses and respiration rates (B), simulated for different sulfate levels and different geologic epochs. The shown profiles were obtained for the same set of model parameter values but with boundary conditions differing among the epochs as indicated in Table 4, for the Fe(III) flux of 63.25 mmol/m<sup>2</sup>/y. Individual model solutions plotted as faint thin lines illustrate the associated variability. Graphs at the bottom indicate the corresponding boundary conditions: concentrations of sulfate and dissolved molecular oxygen in surface water, dissolved iron in the deep ocean reservoir, primary productivity (PP), and the extents of oxygenic versus anoxygenic (iron- or sulfur-based) photosynthesis.

188 We characterize the overall balance between Fe<sup>2+</sup> and H<sub>2</sub>S in the water column by the depth-integrated difference between the  
 189 aqueous sulfide and iron concentrations (Fig. 5B). The distributions of this concentration difference cluster at ± ~10<sup>4</sup> mmol m<sup>-2</sup>,  
 190 corresponding in our simulations (for a 200-m-deep water column) to average concentrations of several tens of μM, and do not  
 191 cover much of the range between these extremes (Fig. 5). In other words, “slightly” ferruginous or euxinic conditions do not appear  
 192 to be stable. The Fe:S stoichiometry of iron sulfide minerals (1:1 for FeS or 1:2 for pyrite) means that the source of the component  
 193 (iron or sulfide) being supplied more quickly cannot be balanced by an iron sulfide precipitation sink. For example, when the net  
 194 sulfide source exceeds the net iron source, precipitation of FeS matches exactly the iron source, while sulfide builds up in the water  
 195 column until its concentration becomes limited by the next most effective sink (e.g., oxidation at the redoxcline) or by the availability  
 196 of organic matter for microbial sulfate reduction.

197 Methanogenesis can occur in water columns below the depths where sulfate is depleted, or in sediments. Importantly, while mi-  
 198 crobial iron reduction becomes more favorable in sediments where Fe(III) and organic substrates are more concentrated, methano-  
 199 genesis can remain sufficiently competitive even under iron-rich conditions (Fig. 2), as is indeed observed in iron-rich lakes<sup>4</sup>. The  
 200 autotrophic anaerobic oxidation of methane by Fe(III) oxides (Fe-dependent AOM), while energetically viable (Fig. 1), becomes com-  
 201 petitively viable only under carbon-limiting conditions, and kinetically significant only in iron-rich environments under very low sul-  
 202 fate (Fig. 1), as recently observed<sup>40</sup>. The S-dependent AOM is energetically inhibited at sulfate levels below several tens of μM (Fig. 1),  
 203 which likely explains the scarcity of observations of this metabolism in lakes<sup>41</sup>, but becomes progressively more favorable at higher  
 204 sulfate concentrations. We note that a complete analysis may need to include hydrogenotrophic pathways. Previous bioenergetics  
 205 modeling suggested that the energetic balance for S-dependent AOM could be controlled by the relative rates of hydrogeotrophic

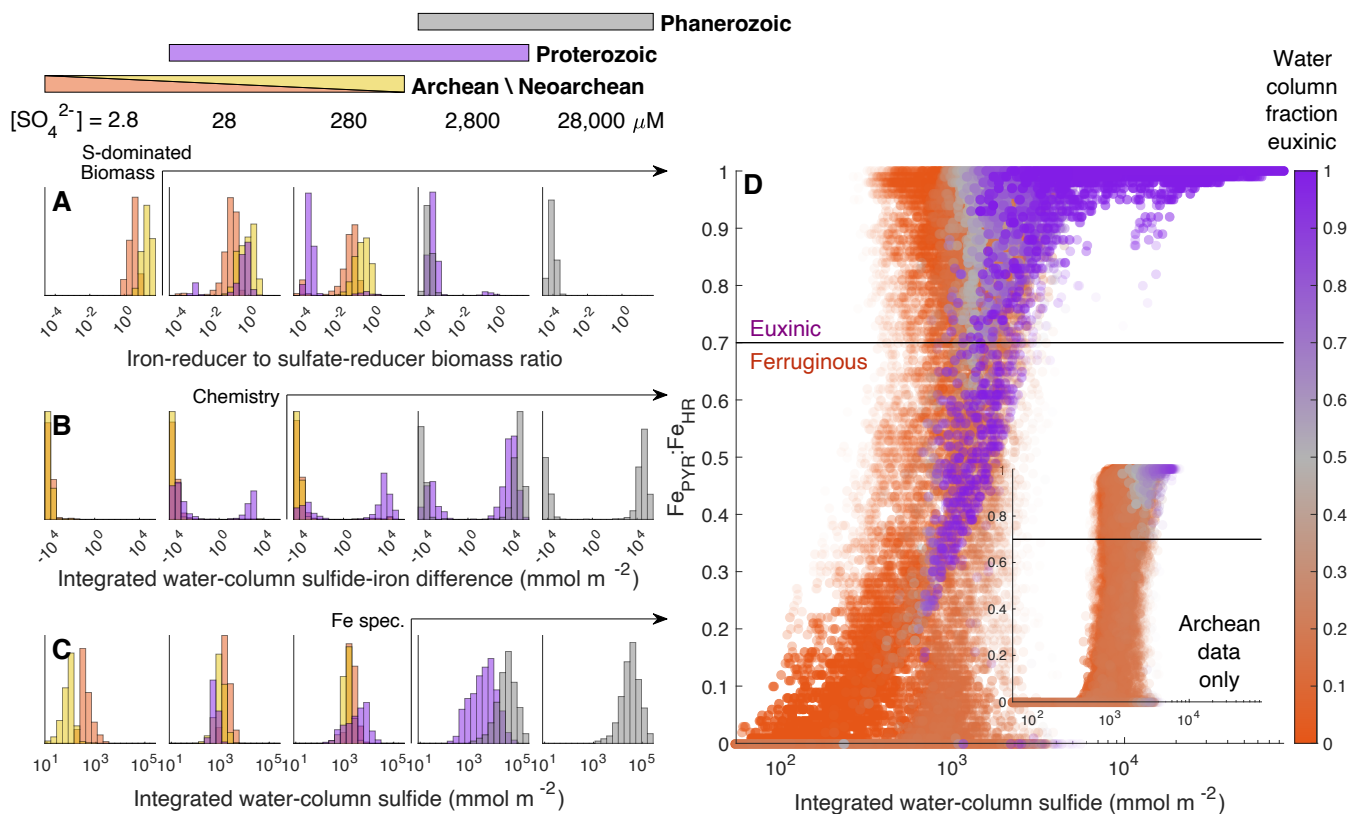


**Figure 5:** Statistics on model solutions, illustrating patterns of microbial activity and water chemistry (A-C), and their manifestations in sediment deposition signals (D). A) Ratios of depth-integrated biomasses of iron reducers to sulfate reducers (see also Fig. S2); B) Depth-integrated difference between the concentrations of total aqueous sulfide and dissolved iron; C) Depth integrated concentrations of total aqueous sulfide (same as the horizontal axis in D; see also Fig. S3); D) Ratios of pyrite to highly reactive iron ( $Fe_{PYR}:Fe_{HR}$ ) in settling particles, against the depth-integrated water-column aqueous sulfide (same as C). Colors represent the fraction of the anoxic water column that is euxinic (defined as sulfide concentrations exceeding ferrous iron concentrations). The line at  $Fe_{PYR}:Fe_{HR}$  of 0.7 is the threshold between ferruginous and euxinic conditions proposed in iron speciation studies<sup>43</sup>. Arrows in panels A-C indicate the points in time (and the corresponding sulfate levels) when sulfate reducers begin to dominate in biomass (A), when sulfide becomes persistent in the water column (B), and when iron speciation in settling particles would begin to be interpreted to reflect euxinic conditions (C). We note that diagenesis in sedimentary rocks from the chemical conditions in the water column<sup>44</sup>.

206 sulfate reduction and acetoclastic methanogenesis, as hydrogen is exchanged between the symbiotic methane-oxidizing archaea  
 207 and SRBs<sup>42</sup>. In carbon-starved environments, such as deep oligotrophic water columns or the deep subsurface, autotrophic path-  
 208 ways (including AOM) become comparatively more competitive (Fig. 1) relative to the heterotrophic pathways with which they com-  
 209 pete for substrates, such as sulfate or iron oxides.

## 210 IMPLICATIONS FOR MODERN AND ANCIENT ENVIRONMENTS

211 In modern oceans, bottom waters are generally oxygenated because meridional overturning supplies  $O_2$  at rates that exceed those  
 212 of aerobic respiration. In restricted basins, such as the Black Sea, Saanich Inlet, or Cariaco Basin<sup>45</sup>, anoxic conditions develop. Our  
 213 one-dimensional model, accordingly, predicts deep-water  $O_2$  depletion even in water bodies with well oxygenated surfaces. In the  
 214 absence of deep-water  $Fe^{2+}$  upwelling, ferruginous conditions can develop only when surface sulfate concentrations are below  
 215  $\sim 100 \mu M$  or the iron supply to the water surface (e.g., as dust or runoff) exceeds hundreds of  $m^{-2} y^{-1}$  (Figs. S4, S5). Under the mod-  
 216 ern high- $O_2$  conditions, this is the case only in a small number of meromictic lakes. Despite only a narrow zone of sulfide accumu-  
 217 lation below the oxycline, sulfate reduction rates in such environments may be substantial (Fig. 3). Except in rare cases of significant  
 218 photoferrotothropy, such as in the Kabuno Bay of Lake Kivu<sup>46</sup>, heterotrophic Fe(III) reduction is limited in the water column (Fig. S6),  
 219 occurring mostly in the sediments. For example, in agreement with our model (Fig. 3), only minimal microbial production of dis-  
 220 solved  $Fe^{2+}$  was suggested for the water column of ferruginous Lake Matano, with most of the  $Fe^{2+}$  coming from benthic fluxes<sup>36</sup>.  
 221 Methanogenesis in such ferruginous environments can be highly active, in agreement with the detection of methanogens in Lake  
 222 Matano<sup>4</sup>, and can account for a large portion of organic carbon mineralization<sup>5</sup>. Despite thermodynamic favorability of Fe-driven

223 AOM, our model suggests relatively low rates of this metabolism, at least in the water column where Fe(III) concentrations are low  
224 (Fig. S7), though we note that its kinetics are poorly constrained. Observational evidence for this pathway so far is circumstantial  
225 and inconclusive. In Lake Matano, for example, mass balance considerations suggested that Fe-AOM may be contributing to water-  
226 column Fe<sup>2+</sup> and serves as a quantitatively important sink for methane in the chemocline<sup>4</sup>, but direct evidence is still lacking. In  
227 neighboring Lake Towuti, in contrast, coexistence of reactive Fe(III) phases with millimolar methane concentrations in sediments  
228 suggested the absence of Fe-driven AOM<sup>5</sup>.

229 Archean oceans are thought to have been characterized by lower-than-present pH and by sulfate concentrations in the low  $\mu\text{M}$  range<sup>47-49</sup>.  
230 Prior to the evolution of oxygenic photosynthesis, primary productivity was sustained by anoxygenic photosynthesis coupled to the  
231 oxidation of either hydrogen sulfide (to elemental sulfur) or Fe<sup>2+</sup> (to Fe(III) oxyhydroxides). The latter process would serve as a source  
232 of highly reactive Fe(III) phases to the water column, supporting iron reduction (Fig. 4). Over the range of parameter values typical of  
233 the Archean, the model predicts that most of the water column remained ferruginous and that degradation of organic matter was  
234 dominated by dissimilatory iron reduction (Figs. 4, S8). Introduction of oxygenic photosynthesis in the Neoproterozoic would further  
235 boost water-column iron reduction by enabling production of reactive Fe(III) particles by oxidation of Fe<sup>2+</sup> upwelled from the ocean  
236 interior. Increases in seawater sulfate during the Neoproterozoic<sup>48</sup> would provide a competing effect, increasing the favorability of dis-  
237 similatory sulfate reduction (Fig. 4). Despite the low sulfate concentrations throughout the Archean, sulfate reduction is predicted  
238 with some parameter combinations to proceed at appreciable rates, with cryptic sulfur cycling supporting respiration of a sizeable  
239 population of microorganisms and accounting for degradation of appreciable fractions of the photosynthetically produced organic  
240 matter (Fig. 4). These predictions are consistent with observations from the modern Lake Towuti, for example, where robust popula-  
241 tions of sulfate reducers were found in sediments underlying a ferruginous water column<sup>50</sup>. Though methanogenesis, even at low  
242 concentrations of sulfate, accounts for a small fraction of the degradation of organic matter (Fig. S9), the depth-integrated rates of  
243 methanogenesis in Archean water columns could be high enough to support large methane fluxes to the atmosphere (Figs. S10,  
244 S11).

245 While modern ferruginous lakes are often construed as geochemical analogues of the Archean oceans<sup>35</sup>, they differ in several im-  
246 portant respects. Anoxygenic photosynthesis in lakes, when present, is relegated to a narrow layer below the oxycline, where regions  
247 of sulfate reduction and iron reduction are separated vertically by density gradients. In the Archean oceans, on the other hand, anoxy-  
248 genic photosynthesis and anaerobic respiration could co-occur in the vigorously mixed surface layer. Reactive Fe(III) oxyhydroxides  
249 would be available throughout the photic zone, where they could support high rates of iron reduction and a substantial biomass of  
250 iron reducers (Fig. 4). Sulfate reduction could take place in the same anoxic mixed layer. At the higher sulfate concentrations that  
251 were likely achieved in the Neoproterozoic<sup>48</sup>, sulfate reducers could dominate the microbial biomass and the respiration of organic  
252 matter, with much of the Fe(III) oxyhydroxides being reduced by microbially generated sulfide rather than via microbial iron reduc-  
253 tion (Fig. 4). Sulfur-based anoxygenic photosynthesis would further consume sulfide, contributing to maintaining a predominantly  
254 ferruginous water column. The biogeochemical and physical settings for the competition between iron reducers and sulfate reduc-  
255 ers in the Archean oceans would thus differ markedly from those in modern ferruginous analogues. Environments that developed  
256 when oxygenic photosynthesis could sustain an oxycline within the water column would resemble modern ferruginous lakes more  
257 closely.

258 Proterozoic oceans are believed to have been characterized by higher primary productivity than in the Archean, sustained predomi-  
259 nantly by oxygenic photosynthesis<sup>51,52</sup>. Sulfate concentrations reached hundreds of  $\mu\text{M}$ <sup>53,54</sup>. The ocean interior is believed to have  
260 remained ferruginous, potentially supplying Fe<sup>2+</sup> to shelf areas by upwelling. Under such conditions, our analysis suggests that sul-  
261 fate reduction would be the dominant pathway of organic carbon mineralization (Fig. 4). At low sulfate concentrations (10s to low  
262 100s of  $\mu\text{M}$ ), methanogenesis could dominate mineralization in deep anoxic waters (Fig. S9), and could sustain noticeable fluxes of  
263 methane even across the oxic surface layer (Fig. S10;<sup>54</sup>). As sulfate levels exceeded 100s of  $\mu\text{M}$ , the dominance of sulfate reduction  
264 would lead to extensive coastal euxinia (Figs. S4, S5). Fluxes of dissolved Fe<sup>2+</sup> from the deep ocean and sediments, however, could  
265 sustain ferruginous conditions in the lower extents of the coastal water columns, potentially affecting diagenetic processes. Under  
266 these conditions, variability in vertical mixing rates, being highly dependent on local hydrodynamic conditions, should have created

267 a large diversity in water chemistry and microbial activity (Figs. 4, 5). This may be reflected in the observed variety in the composi-  
268 tion of Proterozoic sedimentary Fe minerals<sup>55</sup>, though it is unclear that the Fe mineralogy of sedimentary rocks represents water-  
269 column conditions and not diagenetic processes<sup>44,56</sup>.

## 270 INTERPRETATIONS OF SEDIMENT RECORDS

271 While our analysis cannot consider post-depositional alterations of sediments<sup>44,56,57</sup>, it allows us to interpret the depositional sig-  
272 nals that are created by particle fluxes and the degree to which they correspond to chemical conditions in the water column. Even  
273 in the absence of diagenesis, we find that iron speciation, a popular sedimentary proxy of water-column redox conditions<sup>43,58</sup> would  
274 often yield incorrect interpretations (Fig. 5). Specifically, the ratio of pyrite to highly reactive iron ( $\text{Fe}_{\text{PYR}}:\text{Fe}_{\text{HR}}$ ) in particles settling  
275 to the seabed is predicted to be greater than 0.7, the proposed threshold between ferruginous and euxinic water-column chem-  
276 istry, when the total depth-integrated amount of hydrogen sulfide in the water column exceeds  $\sim 1000 \text{ mmol/m}^2$  (Fig. 5). This value  
277 could be typical in the late Archean and early-to-mid Proterozoic, as it corresponds to an average concentration of only  $10 \mu\text{M}$  sul-  
278 fide over a 100-meter water column (Fig. S3). Ferruginous Archean water columns could contain sufficient amounts of sulfide to  
279 pyritize settling particles (Fig. 5), whereas some of the predominantly sulfidic water columns could sustain sufficient downward  
280 fluxes of oxidized iron to generate “ferruginous” diagenetic signals. Even under modern high-sulfate conditions, high Fe(III) fluxes  
281 in oligotrophic (carbon-poor) water columns may result in low  $\text{Fe}_{\text{PYR}}:\text{Fe}_{\text{HR}}$  ratios, analogously to the conditions recorded in the sed-  
282 iments in the Gulf of Acaba<sup>59</sup>. More generally, we find that the main determinant of the degree of sulfidization of sedimentary iron  
283 is not the fraction of the water column occupied by euxinic conditions, but the depth-integrated amount of hydrogen sulfide (Fig.  
284 5C and D).

285 Statistical analyses of our simulations reveal that certain conditions that dominated ancient water columns may have become recorded  
286 in the rock record only in subsequent geological epochs (Fig. 5). For instance, sulfate reducers could dominate the anaerobic respi-  
287 ration already in the ferruginous water columns of the Neoproterozoic, at sulfate levels of only tens of  $\mu\text{M}$ . Euxinia likely became widespread  
288 only during the Proterozoic when sulfate levels reached hundreds of  $\mu\text{M}$ . The euxinic conditions could only be recorded in sediments  
289 (by the  $\text{Fe}_{\text{PYR}}:\text{Fe}_{\text{HR}}$  ratios), however, only at higher sulfate concentrations, when settling particles in Proterozoic or Phanerozoic wa-  
290 ter columns were exposed to higher amounts of sulfide.

291 While alteration of iron speciation in sediments during diagenesis introduces additional effects that are not accounted for by our anal-  
292 ysis, the above examples themselves show that the current interpretive framework based on iron speciation may be insufficient to  
293 constrain the aqueous chemistry even in topmost sediments, especially under mildly (tens of  $\mu\text{M}$ ) sulfidic conditions. More gener-  
294 ally, a more robust definition of ferruginous or euxinic *water columns* (as opposed to the well defined ferruginous or euxinic *condi-*  
295 *tions*) appears to be necessary, given the frequent coexistence of euxinic and ferruginous regions within the same water column.

## 296 IMPLICATIONS FOR MICROBIAL EVOLUTION AND ECOLOGY

297 Anaerobic respiratory pathways evolved on early Earth in ecological niches that were potentially different from those in which they  
298 operate now. Comparing such ecological conditions may hold keys to understanding past and present microbial capabilities. To  
299 sustain their metabolisms, methanogens must extract a high fraction of usable energy out of the small amount of Gibbs free en-  
300 ergy available for their catabolism. Under the ferruginous conditions of early oceans, however, methanogens also had to exist in wa-  
301 ter columns or sediments that contained large amounts of iron. Competing with iron reducers then would require developing fast  
302 turnover rates for organic substrates. This may have allowed methanogens to inhabit substrate-rich ecological niches in upper sedi-  
303 ment and throughout the water column, in contrast to the limited extents of sulfate-free marine columns today. Likewise, sulfate re-  
304 ducers evolved in a low-sulfate world where they had to compete with methanogens and iron reducers. Sulfate reducers could have  
305 initially inhabited the anoxic surface mixed layer where organic matter was more available (Fig. 4) but would then have to adapt to  
306 competing in more limiting conditions once a significant oxic layer developed at the ocean surface (Fig. 4). Sufficiently fast kinetics  
307 of catabolism and an ability to access sulfate at low  $\mu\text{M}$  concentrations gave sulfate reducers the competitive advantage over iron  
308 reducers as soon as sulfate levels increased to even a few tens  $\mu\text{M}$ . From that point onwards, in most marine settings, sulfate reduc-  
309 ers dominated water-column anaerobic populations and respiration rates, whereas the activity of iron reducers was relegated to the

310 sediments.

311 The dynamic stability of the environment also matters for the outcomes of microbial competition. Microbes such as iron reducers,  
312 with high energy yields but low cell-specific rates, respond slowly to changes in their environments. Iron reducers may thus be less  
313 susceptible to transient changes in environmental conditions and may be better adapted to living under more stable conditions  
314 in sediments. Conversely, transient changes in environmental conditions or substrate availability could temporarily lead to domi-  
315 nance of metabolic groups with higher cell-specific catabolic rates, like sulfate reducers and methanogens. Oscillating conditions  
316 could thus lead to dominance of rapidly respiring groups even where the long-term average conditions would lead to dominance of  
317 slower-respiring groups like iron reducers.

318 Our findings also have important implications for genomics-based inferences in aquatic ecology. Biogeochemical cycling is now  
319 routinely informed by abundances of microbial genes and rates of their expression<sup>60</sup>, while geochemical proxies are commonly  
320 viewed as indicative of the activities and dominance of microbial groups. Our results indicate decoupling between the water-column  
321 chemistry and microbial population makeup under certain conditions. For instance, ferruginous conditions do not preclude sub-  
322 stantial activity of sulfate reducers and more generally sulfur cycling, while low cell counts of methanogens may not necessarily in-  
323 dicate the absence of methanogenesis. Such decouplings may thus underlie “cryptic” elemental cycling by detectable, abundant  
324 microorganisms in some cases, and detectable geochemical activities by “stealth” microbial populations in others.

## 325 MATERIALS AND METHODS

### 326 Bioenergetics model

327 The model follows the conceptual approach of Refs. 22,23, which offers one of several ways of addressing metabolic limitations on  
328 microbial kinetics<sup>19</sup>. The net change in the Gibbs free energy of a microbial metabolism (per C-mol of new biomass) is

$$\Delta G = \lambda_{cat} \Delta G_{cat} + \Delta G_{ana} \quad (1)$$

329 where  $\Delta G_{cat}$  and  $\Delta G_{ana}$  are, respectively, the Gibbs free energy of the catabolism and anabolism, and  $\lambda_{cat}$  is the number of times  
330 a catabolic reaction needs to be run to provide the energy needed to form one C-mol of biomass. The maximum growth yield (mol  
331 biomass synthesized per mol reaction) is then

$$Y_{max} = \frac{1}{\lambda_{cat}} = \frac{\Delta G_{cat}}{\Delta G - \Delta G_{ana}} \quad (2)$$

332 We follow the argument of<sup>61</sup> that the Gibbs free energy of a macrochemical reaction  $\Delta G$  is equivalent in magnitude to the dis-  
333 sipated energy  $\Delta G_{dis}$ . The  $\Delta G_{dis}$  was calculated using the phenomenological expression of<sup>61</sup> for heterotrophic and autotrophic  
334 metabolisms.  $\Delta G_{cat}$  and  $\Delta G_{ana}$  were calculated for each individual reaction from the corresponding standard energies of forma-  
335 tion and activity products, at relevant environmental conditions.

336 The cell-specific catabolic rates were calculated as functions of substrate ( $S$ ) concentrations:

$$r = \frac{1}{X} \frac{dS}{dt} = F_K F_T \quad (3)$$

337 Here  $X$  is the biomass in C-mols. The kinetic factor  $F_K$  depends on the pathway-dependent maximum cell-specific rate  $V_{max}$  and  
338 expresses the Monod-type dependence on substrate concentrations:

$$F_K = V_{max} \prod \frac{S_i}{K_m^i + S_i} \quad (4)$$

339 Where oxygen could be present (as in the reaction-transport model described below),  $F_K$  expressions for anaerobic pathways also  
340 included the inhibition factor  $K_{O_2}^{inh} / (K_{O_2}^{inh} + [O_2])$ , to account for oxygen toxicity.

341 The thermodynamic factor  $F_T$  is<sup>62</sup>

$$F_T = 1 - \exp\left(\frac{\Delta G_{cat} + m \Delta G_{ATP}}{\chi RT}\right) \quad (5)$$

342 where  $\Delta G_{ATP}$  is the energy being conserved into ATP, and  $m$  and  $\chi$  are metabolism-specific stoichiometric factors (Table 1). The  
343 evolution of the chemical ( $S$ ) and biomass concentrations ( $X$ ) are then described as:

$$\frac{dS_s}{dt} = A_{sm} r_{mb} X_b + B_{sn} Y_{nm} r_{mb} X_b \quad (6)$$

$$\frac{dX_b}{dt} = \sum_n Y_{nm} r_{mb} X_b - \lambda(m_G) X_b \quad (7)$$

344 Here, summation is implied over the repeating indices (the Einstein convention).  $A_{sm}$  is the stoichiometric matrix for substrate  $s$  in  
345 a catabolic reaction  $m$  catalyzed by the microbial population  $b$ ;  $B_{sn}$  is the stoichiometric matrix for the use of substrate  $s$  in an an-  
346 abolic growth reaction  $n$ ,  $Y_{nm}$  is the yield for the microbial growth utilizing catabolic reaction  $m$  and anabolic reaction  $n$ . The natural  
347 decay of the biomass is described by the "death" term  $\lambda$ , which is a function of the maintenance energy  $m_G$ , which itself depends  
348 on the metabolic power (see SI). For simplicity, in the present model, each catabolic reaction was considered catalyzed by a separate  
349 microbial population, with either heterotrophic or autotrophic anabolism. This approach was used to describe the microbial iron re-  
350 duction (assuming goethite as the reactive solid phase), sulfate reduction, methanogenesis, and Fe- and S-dependent AOM. Kinetic  
351 formulations for other reactions are listed in Table 3.

352 For the flow-reactor mode (Fig. 2), the reactor described by Eqs. 6-7 was allowed to exchange reactive substrates with the ambi-

**Table 1:** Model parameters

| Parameter                     | Value                | Unit   | Range                      | Description and references  |
|-------------------------------|----------------------|--|----------------------------|---|
| $[\text{SO}_4^{2-}]$          |                      | $\mu\text{M}$  | 2.8-28000*                 | surface sulfate concentration   |
| $F_{\text{FeIII}}^0$          |                      | $\text{mmol m}^{-2} \text{y}^{-1}$                           | 1-1500*                    | external flux of particulate Fe(III) (see SI)   |
| $Q_{\text{upwell}}$           |                      | $\text{m y}^{-1}$  | 1-36                       | water upwelling from deep ocean <sup>65</sup>   |
| $\tau_{\text{init}}$          |                      | y  | 0.05-2.0*                  | initial age of organic matter <sup>64,65</sup>  |
| $K_{\text{Ac}}$               | 30                   | $\mu\text{M}$  |                            | acetate half-saturation constant for SR and IR <sup>30,66</sup>   |
|                               | 100                  | $\mu\text{M}$  |                            | acetate half-saturation constant for methanogens <sup>28</sup>  |
| $K_{\text{O}_2}$              | 2                    | $\mu\text{M}$  |                            | oxygen half-saturation constant <sup>67,68</sup>  |
| $K_{\text{O}_2}^{\text{inh}}$ | 1                    | $\mu\text{M}$  |                            | oxygen half-inhibition constant for anaerobes <sup>67,68</sup>  |
| $K_{\text{SO}_4}$             | 5                    | $\mu\text{M}$  |                            | sulfate half-saturation constant for SR <sup>69</sup>   |
| $K_{\text{CH}_4}$             | 30                   | $\mu\text{M}$  |                            | methane half-saturation constant for AOM (see SI)   |
| $K_{\text{FeIII}}$            | 1000                 | $\mu\text{mol/L}$  |                            | goethite half-saturation constant for IR <sup>27</sup>  |
|                               | 10                   | $\mu\text{mol/L}$  |                            | nanophase precipitate half-saturation constant for IR (see SI)  |
| $v_{\text{settle}}$           |                      | $\text{m/y}$   | 100-1000*                  | particle settling velocity <sup>70</sup>  |
| $K_z^0$                       |                      | $\text{m}^2/\text{s}$  | $(0.1-2) \times 10^{-4}$ * | mixing intensity near surface <sup>37,71</sup>  |
| $H_K$                         | 30                   | m  |                            | thermocline depth (for mixing)  |
| $h_K$                         | 7                    | m  |                            | thermocline vertical extent (for mixing)  |
| $f_{Kz}$                      | 0.05                 | -  |                            | ratio of $K_z$ at bottom relative to surface <sup>72</sup>  |
| $f_{\text{rec}}$              |                      | -  | 0-0.5*                     | fraction of Fe(III) recycled in sediments and released to water column  |
| $k_{\text{HSox}}$             | 1                    | $\mu\text{M}^{-1} \text{y}^{-1}$                             |                            | rate constant for sulfide oxidation by oxygen <sup>67</sup>   |
| $k_{\text{Feox}}$             | 1                    | $\mu\text{M}^{-1} \text{y}^{-1}$                             |                            | rate constant for $\text{Fe}^{2+}$ oxidation by oxygen <sup>67</sup>  |
| $k_{\text{HSFeIII}}$          | 0.2                  | $\mu\text{M}^{-1} \text{y}^{-1}$                             |                            | rate constant for sulfide oxidation by Fe(III) (oxyhydr)oxides <sup>67</sup>  |
|                               | 4.0                  | $\mu\text{M}^{-1} \text{y}^{-1}$                             |                            | rate constant for sulfide oxidation by nanophase Fe(III) (oxyhydr)oxides (see SI)   |
| $k_{\text{FeS}}$              | 250                  | $\mu\text{M} \text{y}^{-1}$                                  |                            | rate constant for iron sulfide mineral precipitation <sup>68</sup>  |
| $k_{\text{CH}_4\text{ox}}$    | 1                    | $\mu\text{M}^{-1} \text{y}^{-1}$                             |                            | rate constant for methane oxidation by oxygen <sup>73</sup>   |
| $k_{\text{disp}}$             | 0.02                 | $\text{y}^{-1}$  |                            | rate constant for disproportionation of $\text{S}^0$ <sup>74</sup>  |
| $K_{\text{FeS}}$              | $2.5 \times 10^{-3}$ | M  |                            | equilibrium constant for the reaction $\text{FeS} + \text{H}^+ \rightleftharpoons \text{HS}^- + \text{Fe}^{2+}$ <sup>67</sup> |
| $\Delta G_{\text{ATP}}$       | 30                   | $\text{kJ/mol}$  |                            | cost of producing ATP for $F_T$ ; <sup>75</sup>   |
| $\chi$                        | 8/6/2                | -  |                            | stoichiometric number for IR/SR/MG <sup>3</sup>   |
| $m$                           | 1.25/1/0.25          | -  |                            | stoichiometric number for IR/SR/MG <sup>3</sup>   |
| $V_{\text{max}}$              | 1.0                  | $\text{mol}_{\text{rx}}/\text{mol}_{\text{x}}/\text{h}^{**}$ |                            | microbial kinetics for SR <sup>26</sup>   |
|                               | 0.1/0.3              |  |                            | microbial kinetics for IR <sup>27,31</sup> (bulk/nanophase)   |
|                               | 1.0                  |  |                            | microbial kinetics for MG <sup>26</sup>   |
|                               | 0.04                 |  |                            | microbial kinetics for S-AOM (see SI)   |
|                               | 0.02/0.04            |  |                            | microbial kinetics for Fe-AOM (bulk/nanophase) (see SI)   |
| $\lambda_{\text{death}}$      | $2 \times 10^{-4}$   | $\text{h}^{-1}$  |                            | death rate constant <sup>76</sup>   |
| $k_{\text{death}}$            | $2 \times 10^{-3}$   | $\text{h}^{-1}$  |                            | death rate from energy starvation (see SI))   |
| $[\text{HCO}_3^-]$            | 3                    | mM   |                            | ambient concentration   |
| $[\text{NH}_4^+]$             | 10                   | $\mu\text{M}$  |                            | ambient concentration of nutrient for anabolism   |
| $[\text{H}_2]$                | 0.1                  | $\mu\text{M}$  |                            | ambient concentration   |

Notes: \*Parameter values sampled from uniform distributions of their base-10 logarithms. \*\*Mol-reaction (Table 2) per C-mol of biomass per hour.

ent environment at the rate proportional to the respective concentration differences, with the exchange rate constant of  $0.02 \text{ h}^{-1}$ . Acetate concentrations were imposed in the ambient environment. The model was run to a steady state to obtain the steady-state concentrations of the substrates and the biomasses.

### 356 Reaction-transport model

The one-dimensional reaction transport model solved a system of partial differential equations for a set  $C_j$  of substrate concentrations and biomasses:

$$\frac{\partial C_j}{\partial t} = \frac{\partial}{\partial z} \left( K_z(z) \frac{\partial C_j}{\partial z} \right) - v_j \frac{\partial C_j}{\partial z} + \sum_i \nu_i R_{ij} \quad (8)$$

Here,  $K_z(z)$  is the depth-dependent turbulent eddy diffusion coefficient,  $v_j$  is the settling velocity, and  $R_{ij}$  are the rates of reactions, with stoichiometric coefficients  $\nu_i$ . Explicitly considered concentrations included those of POM, Ac,  $\text{O}_2$ ,  $\text{SO}_4^{2-}$ ,  $\text{H}_2\text{S}_{\text{tot}} = \text{H}_2\text{S} + \text{HS}^-$ ,  $\text{FeOOH}$ ,  $\text{Fe}^{2+}$ ,  $\text{S}^0$ , FeS, and the biomasses of the microbial populations that catalyze the corresponding reactions:  $X_{\text{IR}}$ ,  $X_{\text{SR}}$ ,  $X_{\text{CH}_4}$ ,  $X_{\text{S-AOM}}$ ,  $X_{\text{Fe-AOM}}$ . The concentrations of DIC and ammonium (as the nutrient for anabolism), as well as the pH, were prescribed and assumed constant. The kinetics of the biomass-explicit reactions were simulated as described above for the bioenergetics model. The boundary conditions were prescribed as fixed-concentrations for the dissolved species and fixed-fluxes for the particulate species. A no-gradient boundary condition was imposed at the bottom of the domain, except for species such as  $\text{Fe}^{2+}$  and  $\text{CH}_4$  for which fluxes from sediments could be prescribed, as a fraction of the respective downward fluxes of solid-phase iron and particulate organic matter (POM). The upward flux of  $\text{Fe}^{2+}$  from the ferruginous deep ocean was simulated as an additional flux through the lower domain boundary.

Photosynthetic primary production was assumed to be distributed in the upper water column according to a prescribed (exponen-

**Table 2:** Reactions included in the model. The Gibbs free energy is in units of  $\text{kJ mol}^{-1}$  at pH 7.

| Reaction  | $\Delta G^0$ |
|---|--------------|
| $\text{CO}_2 + \text{H}_2\text{O} + \text{light} \rightarrow \text{POM} + \text{O}_2$   |              |
| $\text{CO}_2 + 4 \text{Fe}^{2+} + 10 \text{H}_2\text{O} + \text{light} \rightarrow \text{POM} + 4 \text{FeOOH} + 8 \text{H}^+$  |              |
| $\text{CO}_2 + 2 \text{H}_2\text{S} + \text{light} \rightarrow \text{POM} + \text{H}_2\text{O} + 2 \text{S}^0$  |              |
| $\text{POM} \rightarrow \text{CH}_3\text{COO}^-$  |              |
| $\text{CH}_3\text{COO}^- + 2 \text{O}_2 \rightarrow 2 \text{HCO}_3^- + \text{H}^+$  | -875         |
| $\text{CH}_3\text{COO}^- + \text{SO}_4^{2-} \rightarrow 2 \text{HCO}_3^- + \text{HS}^-$   | -48          |
| $\text{CH}_3\text{COO}^- + 8 \text{FeOOH} + 15 \text{H}^+ \rightarrow 8 \text{Fe}^{2+} + 2 \text{HCO}_3^- + 12 \text{H}_2\text{O}$  | -132         |
| $\text{CH}_3\text{COO}^- + \text{H}_2\text{O} \rightarrow \text{HCO}_3^- + \text{CH}_4$   | -15          |
| $\text{SO}_4^{2-} + \text{CH}_4 \rightarrow \text{HS}^- + \text{HCO}_3^- + \text{H}_2\text{O}$  | -33          |
| $8 \text{FeOOH} + \text{CH}_4 + 15 \text{H}^+ \rightarrow 8 \text{Fe}^{2+} + \text{HCO}_3^- + 13 \text{H}_2\text{O}$  | -117         |
| $\text{H}_2\text{S} + 2 \text{O}_2 \rightarrow \text{SO}_4^{2-} + 2 \text{H}^+$   | -830         |
| $4 \text{Fe}^{2+} + \text{O}_2 + 6 \text{H}_2\text{O} \rightarrow 4 \text{FeOOH} + 8 \text{H}^+$  | -371         |
| $2 \text{FeOOH} + \text{H}_2\text{S} + 4 \text{H}^+ \rightarrow \text{S}^0 + 2 \text{Fe}^{2+} + 4 \text{H}_2\text{O}$   | -32          |
| $\text{Fe}^{2+} + \text{HS}^- \rightarrow \text{FeS} + \text{H}^+$  |              |
| $4 \text{S}^0 + 4 \text{H}_2\text{O} \rightarrow \text{SO}_4^{2-} + 3 \text{HS}^- + 5 \text{H}^+$   | +55          |
| $0.525 \text{CH}_3\text{COO}^- + 0.2 \text{NH}_4^+ + 0.275 \text{H}^+ \rightarrow$<br>$\rightarrow \text{X}_{\text{hetero}} + 0.05 \text{HCO}_3^- + 0.4 \text{H}_2\text{O}$ | +612         |
| $\text{CO}_2 + 0.2 \text{NH}_4^+ + 0.6 \text{H}_2 \rightarrow \text{X}_{\text{auto}} + 0.2 \text{H}^+ + 1.5 \text{H}_2\text{O}$   | +543         |

**Table 3:** Reaction rate formulations. All reaction rates are in units of  $\mu\text{M y}^{-1}$ .  $R_{PP\text{O}_2}$ ,  $R_{PP\text{Fe}}$  and  $R_{PP\text{H}_2\text{S}}$  are, respectively, the rates of oxygenic, iron-driven anoxygenic, and sulfide-driven anoxygenic photosynthesis (see SI).  $R_G$  is the rate of particulate organic matter (POM) hydrolysis (see SI).  $R_{\text{O}_2}$  is the rate of aerobic respiration.  $R_{\text{HSox}}$ ,  $R_{\text{Feox}}$ , and  $R_{\text{CH}_4\text{ox}}$  are, respectively, the rates of sulfide, ferrous iron, and methane oxidation by oxygen.  $R_{\text{HSFeIII}}$  is the rate of sulfidization of Fe(III) (oxyhydr)oxides.  $R_{\text{FeS}}$  is the rate of FeS precipitation, which depends on the degree of FeS saturation,  $\Omega_{\text{FeS}}$ .  $R_{\text{disp}}$  is the rate of elemental sulfur disproportionation.

| Rate   |
|--|
| $R_{PP\text{O}_2} = R_{PP} \cdot f_{\text{oxygenic}}$  |
| $R_{PP\text{Fe}} = R_{PP} \cdot (1 - f_{\text{oxygenic}}) \frac{[\text{Fe}^{2+}]}{[\text{Fe}^{2+}] + K_{PP\text{Fe}}}$                             |
| $R_{PP\text{H}_2\text{S}} = R_{PP} \cdot (1 - f_{\text{oxygenic}}) \frac{[\Sigma\text{H}_2\text{S}]}{[\Sigma\text{H}_2\text{S}] + K_{PP\text{S}}}$ |
| $R_G = k(z, [\text{O}_2])[\text{POM}]$   |
| $R_{\text{O}_2} = R_G \frac{[\text{O}_2]}{[\text{O}_2] + K_{\text{O}_2}}$  |
| $R_{\text{HSox}} = k_{\text{HSox}} [\Sigma\text{H}_2\text{S}][\text{O}_2]$   |
| $R_{\text{Feox}} = k_{\text{Feox}} [\text{Fe}^{2+}][\text{O}_2]$   |
| $R_{\text{CH}_4\text{ox}} = k_{\text{CH}_4\text{ox}} [\text{CH}_4][\text{O}_2]$  |
| $R_{\text{HSFeIII}} = k_{\text{HSFeIII}} [\text{FeOOH}][\Sigma\text{H}_2\text{S}]$   |
| $R_{\text{FeS}} = k_{\text{FeS}} (\Omega_{\text{FeS}} - 1)$  |
| $\Omega_{\text{FeS}} = \frac{[\text{Fe}^{2+}][\text{HS}^-]}{([\text{H}^+]K_{\text{FeS}})}$   |
| $R_{\text{disp}} = k_{\text{disp}} [\text{S}^0]$   |

370 tial) function of depth, and was assumed to produce POM. Oxygen was produced from that reaction for oxygenic photosynthesis,  
371 whereas anoxygenic pathways produced, respectively, FeOOH and  $\text{S}^0$  (Table 2). The rate of particulate organic carbon mineralization  
372 (hydrolysis) was assumed to follow the power law of Ref. <sup>65</sup>, which stipulates different reactivities under oxic vs. anoxic conditions.  
373 Aerobic respiration was treated as biomass-implicit (no explicit biomass pool), and was assumed to consume acetate at the maxi-  
374 mum rate that matched that of hydrolysis. Precipitation of iron sulfides in the water column was considered to produce FeS. Pyrite  
375 formation was assumed to take place subsequently in the sediment and was not explicitly modelled.

376 The set of equations (8) was solved as an initial-value problem using MATLAB's *pdepe* solver. Solutions were propagated for the sim-  
377 ulation time of 1000 years, with final profiles being used on output as approximations for steady-state solutions.

378 Further details of the model's formulation are provided in the SI. For application of the model to ferruginous Lake Towuti, see Ref. <sup>77</sup>.

### 379 Randomized exploration of model solutions

380 Distributions of model outcomes over a range of environmental conditions were obtained by randomizing model parameters within  
381 their likely ranges, as indicated in Table 1. Parameters were randomly and independently sampled from either uniform or log-uniform  
382 distributions (as indicated in Table 1) to obtain 1000 randomized parameter sets. The same sets were then used to run the model  
383 1000 times for each of the combinations of sulfate concentration levels and Fe(III) fluxes (see supplementary figures) for each of the  
384 geologic epochs. Computations were performed on a parallel computing cluster at the Weizmann Institute of Science.

**Table 4:** Assumed ocean characteristics through time.

| Parameter                                  | Archean | Neoproterozoic       | Proterozoic | Phanerozoic |
|--|---------|----------------------|-------------|-------------|
| T (°C)                                     |         | 4                    | 4           | 4           |
| pH   |         | 6.5                  | 7.5         | 8.0         |
| Surface O <sub>2</sub> (μM)                |         | 2.8×10 <sup>-3</sup> | 28          | 280         |
| Primary Prod. (PP, mmol/m <sup>2</sup> /d) |         | 5-20                 | 25-100      | 50-200      |
| Fraction oxygenic PP                       | 0       | 0.1                  | 1.0         | 1.0         |
| OM settling vel. (m/y)                     |         | 50-100               | 50-100      | 50-100      |
| Deep ocean [Fe <sup>2+</sup> ] (μM)        |         | 100-1,000            | 10-100      | 0           |

### 385 Caveats and limitations

386 The reaction-transport model does not account for the cycling of nitrate or manganese oxides, which were omitted for simplicity.  
 387 These species participate in the organic matter oxidation sequence before iron oxides and sulfate and can also serve as oxidants for  
 388 ferrous iron. While Mn cycling usually happens in a narrow depth interval, in a chemically stratified water column the zone of nitrate  
 389 reduction can be substantial, shifting the zones of iron and sulfate reduction downward. Competitions of these pathways with deni-  
 390 trification, however, merit a separate study. In meromictic Lake Malawi, for example, zones of nitrate reduction and sulfate reduction  
 391 overlap substantially<sup>78</sup>.  
 392 In evaluating the kinetic competitiveness of pathways, we did not model hydrogenotrophic pathways<sup>34</sup>, nor the forward and re-  
 393 verse acetogenesis. These may, in principle, influence metabolic competitiveness under some conditions. We made the choice not  
 394 to include them in this study for reasons of clarity, focusing solely on the competition among the heterotrophic acetate-dependent  
 395 pathways.

### ACKNOWLEDGMENTS

We acknowledge support for a visiting professorship to SK from the De Botton Center for Marine Sciences at the Weizmann Institute of Science, partial support from US NSF grants 1660873 and 1754061 to SK, and the opportunities afforded by the SK's sabbatical leave from the University of Minnesota Duluth.

### REFERENCES

- [1] Ariel D Anbar and Andrew H Knoll. Proterozoic ocean chemistry and evolution: a bioinorganic bridge? *science*, 297(5584):1137–1142, 2002.
- [2] S. W. Poulton and D. E. Canfield. Ferruginous Conditions: A Dominant Feature of the Ocean through Earth's History. *Elements*, 7(2):107–112, apr 2011.
- [3] C. M. Bethke, R. A. Sanford, M. F. Kirk, Q. Jin, and T. M. Flynn. The thermodynamic ladder in geomicrobiology. *American Journal of Science*, 311(3):183–210, mar 2011.
- [4] S.A. Crowe, S. Katsev, K. Leslie, A. Sturm, C. Magen, S. Nomosatryo, M.A. Pack, J.D. Kessler, W.S. Reeburgh, J.A. Roberts, L. González, G. Douglas Haffner, A. Mucci, B. Sundby, and D.A. Fowle. The methane cycle in ferruginous Lake Matano. *Geobiology*, 9(1), 2011.
- [5] André Friese, Kohen Bauer, Clemens Glombitza, Luis Ordoñez, Daniel Ariztegui, Verena B. Heuer, Aurèle Vuillemin, Cynthia Henny, Sulung Nomosatryo, Rachel Simister, Dirk Wagner, Satria Bijaksana, Hendrik Vogel, Martin Melles, James M. Russell, Sean A. Crowe, and Jens Kallmeyer. Organic matter mineralization in modern and ancient ferruginous sediments. *Nature Communications* 2021 12:1, 12(1):1–9, apr 2021.
- [6] Colleen M. Hansel, Chris J. Lentini, Yuanzhi Tang, David T. Johnston, Scott D. Wankel, and Philip M. Jardine. Dominance of sulfur-fueled iron oxide reduction in low-sulfate freshwater sediments. *The ISME Journal* 2015 9:11, 9(11):2400–2412, apr 2015.
- [7] Jasmine S Berg, I D 1d, Jé Zé Quel, Arnaud Duverger, Dominique Lamy, Christel Laberty-Robert, and Jennyfer Miot. Microbial diversity involved in iron and cryptic sulfur cycling in the ferruginous, low-sulfate waters of Lake Pavin. 2019.
- [8] Eric E Roden. Analysis of long-term bacterial vs. chemical Fe (iii) oxide reduction kinetics. *Geochimica et Cosmochimica Acta*, 68(15):3205–3216, 2004.
- [9] Timothy W Lyons, Ariel D Anbar, Silke Severmann, Clint Scott, and Benjamin C Gill. Tracking euxinia in the ancient ocean: a multiproxy perspective and proterozoic case study. *Annual Review of Earth and Planetary Sciences*, 37:507–534, 2009.
- [10] Stephanie L Olson, Christopher T Reinhard, and Timothy W Lyons. Limited role for methane in the mid-proterozoic greenhouse. *Proceedings of the National Academy of Sciences*, 113(41):11447–11452, 2016.
- [11] Elizabeth D. Swanner, Nicholas Lambrecht, Chad Wittkop, Chris Harding, Sergei Katsev, Joshua Torgeson, and Simon W. Poulton. The biogeochemistry of ferruginous lakes and past ferruginous oceans. *Earth-Science Reviews*, 211:103430, dec 2020.
- [12] S. Katsev, I. Tsandev, I. L'Heureux, and D.G. Rancourt. Factors controlling long-term phosphorus efflux from lake sediments: Exploratory reactive-transport modeling. *Chemical Geology*, 234(1-2), 2006.
- [13] I Halevy, DA Fike, V Pasquier, RN Bryant, CB Wenk, AV Turchyn, DT Johnston, and GE Claypool. Sedimentary parameters control the sulfur isotope composition of marine pyrite. *Science*, 382(6673):946–951, 2023.
- [14] A. W. Dale, P. Van Cappellen, D. R. Aguilera, and P. Regnier. Methane efflux from marine sediments in passive and active margins: Estimations from bioenergetic reaction-transport simulations. *Earth and Planetary Science Letters*, 265(3-4):329–344, jan 2008.
- [15] Christof Meile and Timothy D Scheibe. Reactive transport modeling of microbial dynamics. *Elements: An International Magazine of Mineralogy, Geochemistry, and Petrology*, 15(2):111–116, 2019.
- [16] Daniel C. Reed, Christopher K. Algar, Julie A. Huber, and Gregory J. Dick. Gene-centric approach to integrating environmental genomics and biogeochemical models. *Proceedings of the National Academy of Sciences of the United States of America*, 111(5):1879–1884, feb 2014.
- [17] S. Louca, A.K. Hawley, S. Katsev, M. Torres-Beltran, M.P. Bhatia, S. Kheirandish, C.C. Michiels, D. Capelle, G. Lavik, M. Doebeli, S.A. Crowe, and S.J. Hallam. Integrating biogeochemistry with multiomic sequence information in a model oxygen minimum zone. *Proceedings of the National Academy of Sciences of the United States of America*, 113(40), 2016.
- [18] A. W. Dale, P. Regnier, and P. Van Cappellen. Bioenergetic Controls on Anaerobic Oxidation of Methane (AOM) in Coastal Marine Sediments: A Theoretical Analysis. *American Journal of Science*, 306(4):246–294, apr 2006.
- [19] Qusheng Jin. Building microbial kinetic models for environmental application: A theoretical perspective. *Applied Geochemistry*, page 105782, 2023.
- [20] Jin Qusheng and Craig M Bethke. Predicting the rate of microbial respiration in geochemical environments. 2005.
- [21] Urs Von Stockar, Thomas Maskow, Jingsong Liu, Ian W Marison, and Rodrigo Patiño. Thermodynamics of microbial growth and metabolism: An analysis of the current situation. *Journal of Biotechnology*, 121:517–533, 2006.
- [22] Rebeca González-Cabaleiro, Irina D Ofit'yeru, Juan M Lema, and Jorge Rodríguez. Microbial catabolic activities are naturally selected by metabolic energy harvest rate. *The ISME Journal*, 9:2630–2641, 2016.
- [23] Christina M Smeaton and Philippe Van Cappellen. Gibbs Energy Dynamic Yield Method (GEDYM): Predicting microbial growth yields under energy-limiting conditions. *Geochimica et Cosmochimica Acta*, 241:1–16, nov 2018.
- [24] Qiong Wu, Megan J Guthrie, and Qusheng Jin. Physiological acclimation extrapolates the kinetics and thermodynamics of methanogenesis from laboratory experiments to natural environments. *Frontiers in Ecology and Evolution*, 10:838487, 2022.
- [25] Eric E Roden and John M Zachara. Microbial reduction of crystalline iron (iii) oxides: influence of oxide surface area and potential for cell growth. *Environmental Science & Technology*, 30(5):1618–1628, 1996.
- [26] Johannes CM Scholten, Peter M van Bodegom, Jaap Vogelaar, Alexander van Ittersum, Kees Hordijk, Wim Roelofsen, and Alfons JM Stams. Effect of sulfate and nitrate on acetate conversion by anaerobic microorganisms in a freshwater sediment. *FEMS Microbiology Ecology*, 42(3):375–385, 2002.
- [27] Steeve Bonneville, Philippe Van Cappellen, and Thilo Behrends. Microbial reduction of iron(III) oxyhydroxides: effects of mineral solubility and availability. 2004.

- [28] AJM Stams, Caroline M Plugge, Frank AM De Bok, BHGW Van Houten, Piet Lens, H Dijkman, and Jan Weijma. Metabolic interactions in methanogenic and sulfate-reducing bioreactors. *Water Science and Technology*, 52(1-2):13–20, 2005.
- [29] Derek R Lovley and Michael J Klug. Sulfate reducers can outcompete methanogens at freshwater sulfate concentrations. *Applied and Environmental Microbiology*, 45(1):187–192, 1983.
- [30] Eric E Roden and RG Wetzel. Competition between Fe(III)-reducing and methanogenic bacteria for acetate in iron-rich freshwater sediments. *Microbial Ecology*, 45(3):252–258, 2003.
- [31] Christelle Hyacinthe, Steve Bonneville, and Philippe Van Cappellen. Reactive iron (III) in sediments: chemical versus microbial extractions. *Geochimica et Cosmochimica Acta*, 70(16):4166–4180, 2006.
- [32] Silke Schulz and Ralf Conrad. Effect of algal deposition on acetate and methane concentrations in the profundal sediment of a deep lake (lake Constance). *FEMS microbiology ecology*, 16(4):251–259, 1995.
- [33] Clemens Glombitza, Marion Jaussi, Hans Røy, Marit-Solveig Seidenkrantz, Bente A Lomstein, and Bo B Jørgensen. Formate, acetate, and propionate as substrates for sulfate reduction in sub-arctic sediments of southwest Greenland. *Frontiers in Microbiology*, 6:846, 2015.
- [34] F Beulig, H Røy, C Glombitza, B B Jørgensen, and David M Karl. Control on rate and pathway of anaerobic organic carbon degradation in the seabed. 2018.
- [35] S.A. Crowe, C. Jones, S. Katsev, C. Magen, A.H. O'Neill, A. Sturm, D.E. Canfield, G.D. Haffner, A. Mucci, B. Sundby, and D.A. Fowle. Photoferrotrophs thrive in an Archean Ocean analogue. *Proceedings of the National Academy of Sciences of the United States of America*, 105(41), 2008.
- [36] S.A. Crowe, A.H. O'Neill, S. Katsev, P. Hehanussa, G.D. Haffner, B. Sundby, A. Mucci, and D.A. Fowle. The biogeochemistry of tropical lakes: A case study from Lake Matano, Indonesia. *Limnology and Oceanography*, 53(1), 2008.
- [37] S. Katsev, S.A. Crowe, A. Mucci, B. Sundby, S. Nomosatryo, G. Douglas Haffner, and D.A. Fowle. Mixing and its effects on biogeochemistry in the persistently stratified, deep, tropical Lake Matano, Indonesia. *Limnology and Oceanography*, 55(2), 2010.
- [38] Chad Wittkop, Elizabeth D Swanner, Ashley Grengs, Nicholas Lambrecht, Mojtaba Fakhræe, Amy Myrbo, Andrew W Bray, Simon W Poulton, and Sergei Katsev. Evaluating a primary carbonate pathway for manganese enrichments in reducing environments. *Earth and Planetary Science Letters*, 538:116201, 2020.
- [39] Sergei Katsev, Piet Verburg, Marc Lirós, Elizabeth C Minor, Brittany R Kruger, and Jiyng Li. Tropical meromictic lakes: specifics of meromixis and case studies of lakes Tanganyika, Malawi, and Matano. In *Ecology of meromictic lakes*, pages 277–323. Springer, 2017.
- [40] David A. Aromokaye, Ajinkya C. Kulkarni, Marcus Elvert, Gunter Wegener, Susann Henkel, Sarah Coffinet, Thilo Eickhorst, Oluwatobi E. Oni, Tim Richter-Heitmann, Annika Schnakenberg, Heidi Taubner, Lea Wunder, Xiuran Yin, Qingzeng Zhu, Kai Uwe Hinrichs, Sabine Kasten, and Michael W. Friedrich. Rates and Microbial Players of Iron-Driven Anaerobic Oxidation of Methane in Methanic Marine Sediments. *Frontiers in Microbiology*, 10:3041, Jan 2020.
- [41] Edith Durisch-Kaiser, Martin Schmid, Frank Peeters, Rolf Kipfer, Christian Dinkel, Torsten Diem, Carsten J Schubert, and Bernhard Wehrl. What prevents outgassing of methane to the atmosphere in lake Tanganyika? *Journal of Geophysical Research: Biogeosciences*, 116(G2), 2011.
- [42] A W Dale, P Regnier, and P Van Cappellen. BIOENERGETIC CONTROLS ON ANAEROBIC OXIDATION OF METHANE (AOM) IN COASTAL MARINE SEDIMENTS: A THEORETICAL ANALYSIS.
- [43] Simon W Poulton. *The iron speciation paleoredox proxy*. Cambridge University Press, 2021.
- [44] V Pasquier, DA Fike, Sidonie Révillon, and I Halevy. A global reassessment of the controls on iron speciation in modern sediments and sedimentary rocks: A dominant role for diagenesis. *Geochimica et Cosmochimica Acta*, 335:211–230, 2022.
- [45] Thomas J Algeo and Chao Li. Redox classification and calibration of redox thresholds in sedimentary systems. *Geochimica et Cosmochimica Acta*, 287:8–26, 2020.
- [46] Marc Lirós, Tamara García-Armisen, François Darchambeau, Cédric Morana, Xavier Triadó-Margarit, Özgül Inceolu, Carles M. Borrego, Steven Bouillon, Pierre Servais, Alberto V. Borges, Jean Pierre Descy, Don E. Canfield, and Sean A. Crowe. Pelagic photoferritrophy and iron cycling in a modern ferruginous basin. *Scientific Reports*, 5, Sep 2015.
- [47] I Halevy and A Bachan. The geologic history of seawater pH. *Science (New York, N.Y.)*, 355(6329):1069–1071, Mar 2017.
- [48] M. Fakhræe, S.A. Crowe, and S. Katsev. Sedimentary sulfur isotopes and neoproterozoic ocean oxygenation. *Science Advances*, 4(1):e1701835, 2018.
- [49] S.A. Crowe, G. Paris, S. Katsev, C. Jones, S.-T. Kim, A.L. Zerkle, S. Nomosatryo, D.A. Fowle, J.F. Adkins, A.L. Sessions, J. Farquhar, and D.E. Canfield. Sulfate was a trace constituent of Archean seawater. *Science*, 346(6210), 2014.
- [50] Aurèle Vuillemin, Fabian Horn, André Friese, Matthias Winkel, Mashal Alawi, Dirk Wagner, Cynthia Henny, William D Orsi, Sean A Crowe, and Jens Kallmeyer. Metabolic potential of microbial communities from ferruginous sediments. *Environmental Microbiology*, 20(12):4297–4313, 2018.
- [51] Peter W Crockford, Justin A Hayles, Huiming Bao, Noah J Planavsky, Andrey Bekker, Philip W Fralick, Galen P Halverson, Thi Hao Bui, Yongbo Peng, and Boswell A Wing. Triple oxygen isotope evidence for limited mid-proterozoic primary productivity. *Nature*, 559(7715):613–616, 2018.
- [52] Peter W Crockford, Yinyin M Bar On, Luca M Ward, Ron Milo, and Itay Halevy. The geologic history of primary productivity. *Current Biology*, 33(21):4741–4750, 2023.
- [53] Noah J Planavsky, Andrey Bekker, Axel Hofmann, Jeremy D Owens, and Timothy W Lyons. Sulfur record of rising and falling marine oxygen and sulfate levels during the lomagundi event. *Proceedings of the National Academy of Sciences*, 109(45):18300–18305, 2012.
- [54] Mojtaba Fakhræe, Olivier Hancisse, Donald E. Canfield, Sean A. Crowe, and Sergei Katsev. Proterozoic seawater sulfate scarcity and the evolution of ocean-atmosphere chemistry. *Nature Geoscience*, 12(5):375–380, May 2019.
- [55] Noah J Planavsky, Peter McGoldrick, Clinton T Scott, Chao Li, Christopher T Reinhard, Amy E Kelly, Xuelei Chu, Andrey Bekker, Gordon D Love, and Timothy W Lyons. Widespread iron-rich conditions in the mid-proterozoic ocean. *Nature*, 477(7365):448–451, 2011.
- [56] Alec M Hutchings and Alexandra V Turchyn. A quantification of the effect of diagenesis on the paleoredox record in mid-proterozoic sedimentary rocks. *Geology*, 49(9):1143–1147, 2021.
- [57] Dalton S Hardisty, Timothy W Lyons, Natascha Riedinger, Terry T Isson, Jeremy D Owens, Robert C Aller, Danny M Rye, Noah J Planavsky, Christopher T Reinhard, Ben C Gill, et al. An evaluation of sedimentary molybdenum and iron as proxies for pore fluid paleoredox conditions. *American Journal of Science*, 318(5):527–556, 2018.
- [58] Rob Raiswell, Dalton S Hardisty, Timothy W Lyons, Donald E Canfield, Jeremy D Owens, Noah J Planavsky, Simon W Poulton, and Christopher T Reinhard. The iron paleoredox proxies: A guide to the pitfalls, problems and proper practice. *American Journal of Science*, 318(5):491–526, 2018.
- [59] Valeria Boyko, Barak Blonder, and Alexey Kamysny Jr. Sources and transformations of iron in the sediments of the gulf of aqaba (red sea). *Marine Chemistry*, 216:103691, 2019.
- [60] Hans-Peter Grossart, Ramon Massana, Katherine D McMahon, and David A Walsh. Linking metagenomics to aquatic microbial ecology and biogeochemical cycles. *Limnology and Oceanography*, 65:52–520, 2020.
- [61] J.J. Heijnen and J.P. Van Dijken. In search of a thermodynamic description of biomass yields for the chemotrophic growth of microorganisms. *Biotechnology and Bioengineering*, 39(8):833–858, Apr 1992.
- [62] Q. Jin and C. M. Bethke. The thermodynamics and kinetics of microbial metabolism. *American Journal of Science*, 307(4):643–677, Apr 2007.
- [63] Gary Froyland, Robyn M Stuart, and Erik van Sebille. How well-connected is the surface of the global ocean? *Chaos: An Interdisciplinary Journal of Nonlinear Science*, 24(3), 2014.
- [64] Jack J Middelburg. A simple rate model for organic matter decomposition in marine sediments. *Geochimica et Cosmochimica Acta*, 53(7):1577–1581, 1989.
- [65] S. Katsev and S.A. Crowe. Organic carbon burial efficiencies in sediments: The power law of mineralization revisited. *Geology*, 43(7), 2015.
- [66] Tung-Yuan Ho, Mary I Scranton, Gordon T Taylor, Ramon Varela, Robert C Thunell, and Frank Muller-Karger. Acetate cycling in the water column of the Cariaco basin: seasonal and vertical variability and implication for carbon cycling. *Limnology and Oceanography*, 47(4):1119–1128, 2002.
- [67] S. Katsev, G. Chaillou, B. Sundby, and A. Mucci. Effects of progressive oxygen depletion on sediment diagenesis and fluxes: A model for the lower St. Lawrence River Estuary. *Limnology and Oceanography*, 52(6), 2007.
- [68] S. Katsev, D.G. Rancourt, and I. L'Heureux. dSED: A database tool for modeling sediment early diagenesis. *Computers and Geosciences*, 30(9-10), 2004.
- [69] Irene Harder Tarpgaard, Hans Røy, and Bo Barker Jørgensen. Concurrent low- and high-affinity sulfate reduction kinetics in marine sediment. *Geochimica et Cosmochimica Acta*, 75(11):2997–3010, 2011.
- [70] Cindy Lee, Michael L. Peterson, Stuart G. Wakeham, Robert A. Armstrong, J. Kirk Cochran, Juan Carlos Miquel, Scott W. Fowler, David Hirschberg, Aaron Beck, and Jianhong Xue. Particulate organic matter and ballast fluxes measured using time-series and settling velocity sediment traps in the northwestern Mediterranean Sea. *Deep-Sea Research Part II: Topical Studies in Oceanography*, 56(18):1420–1436, Aug 2009.
- [71] Claudia R Benitez-Nelson, Ken O Buesseler, and Glenn Crossin. Upper ocean carbon export, horizontal transport, and vertical eddy diffusivity in the southwestern Gulf of Maine. *Continental Shelf Research*, 20(6):707–736, 2000.
- [72] MC Gregg. Diapycnal mixing in the thermocline: A review. *Journal of Geophysical Research: Oceans*, 92(C5):5249–5286, 1987.
- [73] Eric W Chan, Allan M Shiller, Dongjoo J Joung, Eleanor C Arrington, David L Valentine, Molly C Redmond, John A Breier, Scott A Socolofsky, and John D Kessler. Investigations of aerobic methane oxidation in two marine seep environments: Part I chemical kinetics. *Journal of Geophysical Research: Oceans*, 124(12):8852–8868, 2019.
- [74] M. Fakhræe, J. Li, and S. Katsev. Significant role of organic sulfur in supporting sedimentary sulfate reduction in low-sulfate environments. *Geochimica et Cosmochimica Acta*, 213:502–516, 2017.
- [75] Moritz E Beber, Mattia G Gollub, Dana Mozaffari, Kevin M Shebek, Avi I Flamholz, Ron Milo, and Elad Noor. eQuilibrator 3.0: a database solution for thermodynamic constant estimation. *Nucleic acids research*, 50(D1):D603–D609, 2022.
- [76] William R Shoemaker, Stuart E Jones, Mario E Muscarella, Megan G Behringer, Brent K Lehmkuhl, and Jay T Lennon. Microbial population dynamics and evolutionary outcomes under extreme energy limitation. *Proceedings of the National Academy of Sciences*, 118(33):e2101691118, 2021.
- [77] Tongyao Pu, G Douglas Haffner, Sean A Crowe, and Sergei Katsev. Stratification stability of tropical lakes and their sensitivity to climate. *Limnology Oceanography*, 2025.
- [78] J. Li, E.T. Brown, S.A. Crowe, and S. Katsev. Sediment geochemistry and contributions to carbon and nutrient cycling in a deep meromictic tropical lake: Lake Malawi (East Africa). *Journal of Great Lakes Research*, 2018.
- [79] L. Tjihuis, M. C.M. Van Loosdrecht, and J. J. Heijnen. A thermodynamically based correlation for maintenance Gibbs energy requirements in aerobic and anaerobic chemotrophic growth. *Biotechnology and Bioengineering*, 42(4):509–519, Aug 1993.
- [80] Kohen W Bauer, Cinzia Bottini, Sergei Katsev, Mark Jellinek, Roger Francois, Elisabetta Erba, and Sean A Crowe. Ferruginous oceans during oae1a and collapse of the marine sulfate pool. *Earth and Planetary Science Letters*, 578:117324, 2022.
- [81] Yibin Huang, David Nicholson, Bangqin Huang, and Nicolas Cassar. Global estimates of marine gross primary production based on machine learning upscaling of field observations. *Global Biogeochemical Cycles*, 35(3):e2020GB006718, 2021.

## SUPPORTING INFORMATION

### Additional details of model formulation

In the bioenergetics model, the microbial death term was described as

$$\lambda(m_G) = \lambda_{death} - \min \left[ 0, k_{death} \left( \frac{rF_T \Delta G_{cat}}{P_{maint}} - 1 \right) \right] \quad (9)$$

This formulation accounts for an increased rate of cell death when the obtained catabolic power falls below the minimum maintenance power requirement  $P_{maint}$ , as well as a lower, uniform death rate  $\lambda_{death}$  from viral lysis, etc. The maintenance power (kJ/mol<sub>x</sub>/h) was calculated as a function of absolute temperature according to Ref.<sup>79</sup>:

$$P_{maint} = 4.5 \exp \left[ -\frac{69}{R} \left( \frac{1}{T} - \frac{1}{298} \right) \right] \quad (10)$$

Anabolism was assumed to slow down at very low concentrations of acetate (as a carbon source), which was described by a Monod-type kinetic term with the half-saturation constant  $K_{ana} = 0.01 \mu\text{M}$ .

In the reaction-transport model, the depth variation in mixing by turbulent eddy diffusion was simulated according to

$$K_z(z) = K_z^0 \left( f_{Kz} + \frac{1 - f_{Kz}}{1 + e^{(z-H_K)/h_K}} \right) \quad (11)$$

This mimics the greater intensity of mixing in the surface waters about the thermocline, though it does not account for a potential increase in mixing below the thermocline, which can result from a weaker density gradient there<sup>37</sup>.

The depth distribution of photosynthetic primary production was described as

$$R_{PP}(z) = \frac{2PP}{\sigma\sqrt{2\pi}} e^{-z^2/2\sigma^2}; \quad (12)$$

where the half-width  $\sigma$  was set to  $H_K/2$ . The integral of this function over depth equals  $PP$ .

The reactivity of POM was described as a function of the ambient oxygen concentration and the age of organic material:

$$k(z, [O_2]) = f k_{ox} + (1 - f) k_{anox} \quad (13)$$

where the partitioning coefficient is  $f = [O_2]/(K_{O_2} + [O_2])$ . The reactivities for the oxic and anoxic mineralization are<sup>65</sup>:

$$k_{ox} = 10^{-0.312\tau - 0.977} \quad (14)$$

$$k_{anox} = 10^{-1.1\tau - 0.857} \quad (15)$$

where the age  $\tau$  of organic material (in years) was calculated at each depth as

$$\tau = \tau_{init} + \int_0^z \frac{dz}{v_{diff} + v_{settleG}} \quad (16)$$

The effective downward velocity  $v_{diff} = d\bar{z}/dt$  due to turbulent diffusion here reflects the root-mean-square displacement that in a diffusive process increases as a square root of time  $\bar{z} = \sqrt{2K_z t}$ ; it was calculated accordingly as

$$v_{diff} = \frac{1}{\frac{z}{K_z} - \left(\frac{z}{2K_z}\right)^2 \frac{dK_z}{dz}} \quad (17)$$

The supply of  $\text{Fe}^{2+}$  from the deep ocean by upwelling was calculated as a flux across the bottom boundary of the model that is proportional to the  $\text{Fe}^{2+}$  concentration difference between the bottom waters and the deeper ocean:

$$F_{Fe-upwell} = ([\text{Fe}^{2+}]_{deep} - [\text{Fe}^{2+}]_{bot}) Q_{upwell} \quad (18)$$

The flux of  $\text{Fe}^{2+}$  from sediments was assumed to be zero under oxic ( $\text{O}_2 > 0.1 \mu\text{M}$ ) or sulfidic ( $\text{H}_2\text{S} > 1 \mu\text{M}$ ) bottom conditions. Otherwise, it was calculated from the near-bottom downward flux of particulate iron  $F_{FeIII}$  according to the specified efficiency of recycling  $f_{rec}$ , up to a maximum imposed by the available flux  $F_{OM}$  of settling organic matter and the 1 : 4 stoichiometry of dissimilatory iron reduction:

$$F_{Fe-sed} = f_{rec} F_{FeIII} \min \left[ 1, \frac{F_{OM}}{4F_{FeIII}} \right] \quad (19)$$

### Simulations of Lake Matano

Lake-specific parameters used in the model included upper boundary conditions for dissolved oxygen and sulfate. The intensity of vertical mixing was specified as a function of depth according to<sup>37</sup>. Model parameters adjusted to reflect broadly in-lake conditions<sup>4,35,36,80</sup> included:  $F_{FeIII}^0 = 240 \text{ mmol/m}^2/\text{y}$ ,  $PP = 150 \text{ mmol/m}^2/\text{d}$ ,  $v_{settle} = 1800 \text{ m/y}$ ,  $v_{OM} = 666 \text{ m/y}$ ,  $H_K = 88 \text{ m}$ ,  $h_K = 6 \text{ m}$ ,  $f_{rec} = 0.35$ ,  $\text{pH} = 7.2$ ,  $T = 29^\circ\text{C}$ . Organic matter reaching the sediment was considered to be recycled into methane fluxing back into the water column with the efficiency of 37%.

As already noted in early work on Lake Matano<sup>36</sup>, geochemical distributions in the water column are shaped primarily by physical mixing, with chemical sources and sinks contributing at the top and bottom boundaries and the relatively narrow chemocline. The chemical reactions in the bulk monimolimnion are thus only weakly constrained by the data, so the corresponding model results should be treated as illustration of the likely patterns, rather than their quantification.

### Additional justification of model parameters

Model parameters in Table 1 were chosen to represent most likely conditions for coastal marine environments. Parameter ranges for the sensitivity analysis (Table 1) were chosen to bracket the corresponding likely ranges over the simulated geologic periods. As true probability distributions over time and space are not known, we used uniform distributions, either of the parameter values themselves or of their logarithms (in cases where likely values spanned several orders of magnitude). The obtained distributions of model solutions thus should not be viewed as approximations for the corresponding true probabilities. The ranges of model solutions are expected to span the corresponding true ranges, however. Information below provides additional context for values and ranges in Table 1.

External fluxes of particulate iron,  $F_{FeIII}^0$ , with runoff and dust deposition in modern high-iron environments can reach several 100s  $\text{mmol m}^{-2} \text{y}^{-1}$ <sup>59,80</sup>. Typical coastal environments, especially under low-oxygen conditions, likely had values closer to the lower end of our chosen range ( $1\text{-}1500 \text{ mmol m}^{-2} \text{y}^{-1}$ ), whereas values at the top of the range could represent more extreme or possibly more land-influenced environments, similar to modern small ferruginous lakes<sup>11</sup>. Gross primary production for coastal ocean settings (Table 4) was taken from the modern ocean value of around  $100 \text{ mmol/m}^2/\text{d}$ <sup>81</sup> and scaled down for earlier geologic epochs in line with current understanding<sup>52</sup>.

Values for several parameters that describe microbial kinetics and are still poorly constrained by available data were chosen as best guesses. They included the Monod-type half-saturation constant  $K_{CH4}$  for methane oxidation by AOM consortia, the maximum cell-specific catabolic rates ( $V_{max}$ ) for both S- and Fe-driven AOM, and the cell death parameter  $k_{death}$ . The Monod half-saturation constant  $K_{FeIII}$  for reduction of nanophase (freshly precipitated) iron oxyhydroxides was chosen to be much lower than the corresponding parameter for crystalline Fe(III) phases (Table 1), to reflect their greater availability to microbial cells and the known reduction of such particles at  $\mu\text{M}$  concentrations in ferruginous chemoclines<sup>80</sup>. Similarly, the rate of abiotic oxidation of hydrogen sulfide at the surface of such particles ( $k_{HSFeIII}$ ) was assumed to be higher than for crystalline oxides, to reflect the greater specific surface area.

## SUPPLEMENTARY FIGURES

Figures below show the results of model exploration for different geologic eons, for the specified discrete levels of sulfate concentrations and Fe(III) inputs at the upper model boundary. The values for the sulfate concentrations and Fe(III) fluxes are shown in the lower row and the rightmost column, respectively. Histograms for quantities specified in the figure captions were obtained by randomized model runs, as described in the Methods section. Histogram colors correspond to the geologic periods (Archean = orange; Neoproterozoic = yellow; Proterozoic = purple; Phanerozoic = grey). The colored bars at the top extend over the sulfate concentrations that may be considered plausible for the corresponding eons.

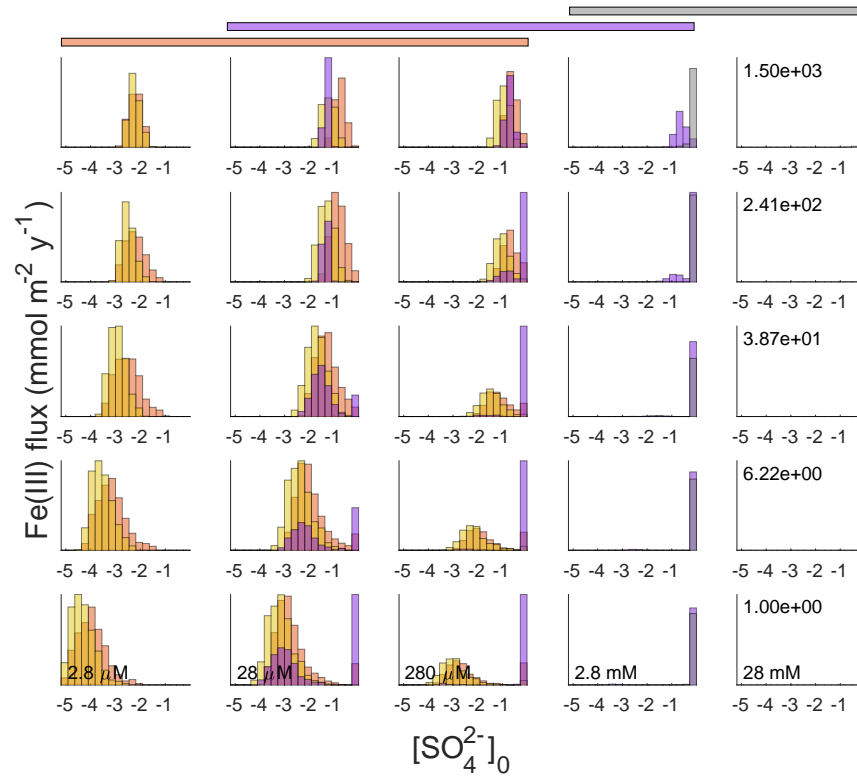


**Fig. S1.** Ratio of the depth-integrated rate of abiotic iron reduction driven by dissolved hydrogen sulfide to the depth-integrated rate of microbial iron reduction ( $R_{HSFeIII} : R_{IR}$ ), on a logarithmic scale. Values smaller than zero indicate dominance of abiotic S-dependent reduction of iron in the water column.

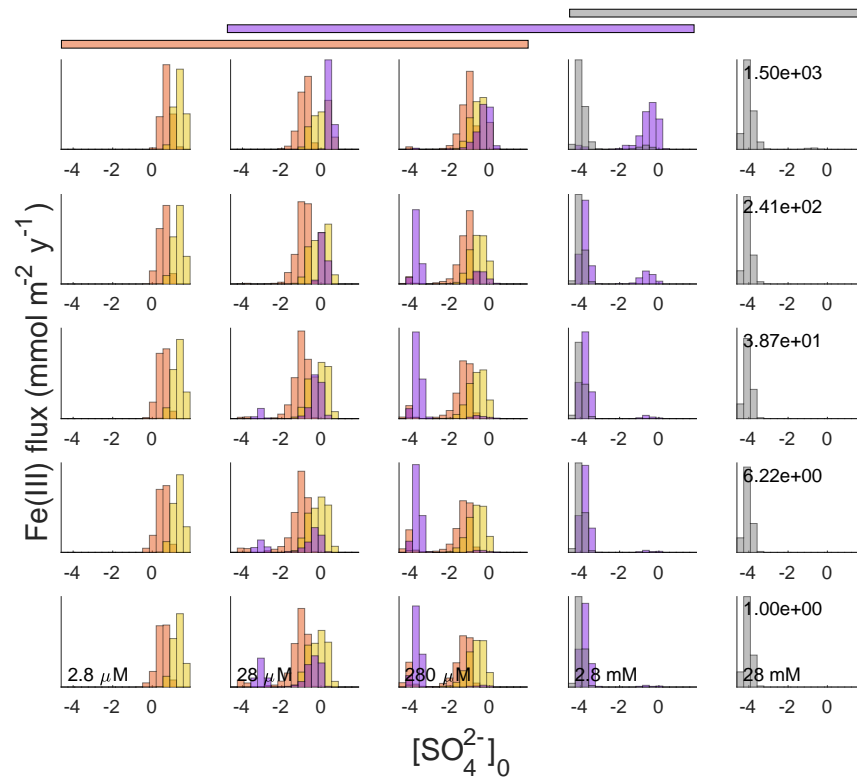


**Fig. S2.** Ratio of the depth-integrated biomasses of iron reducers and sulfate reducers ( $\Sigma X_{IR} : \Sigma X_{SR}$ ), on a logarithmic scale. Values greater than zero indicate dominance of iron reduction. Values smaller than zero indicate dominance of sulfate reduction.

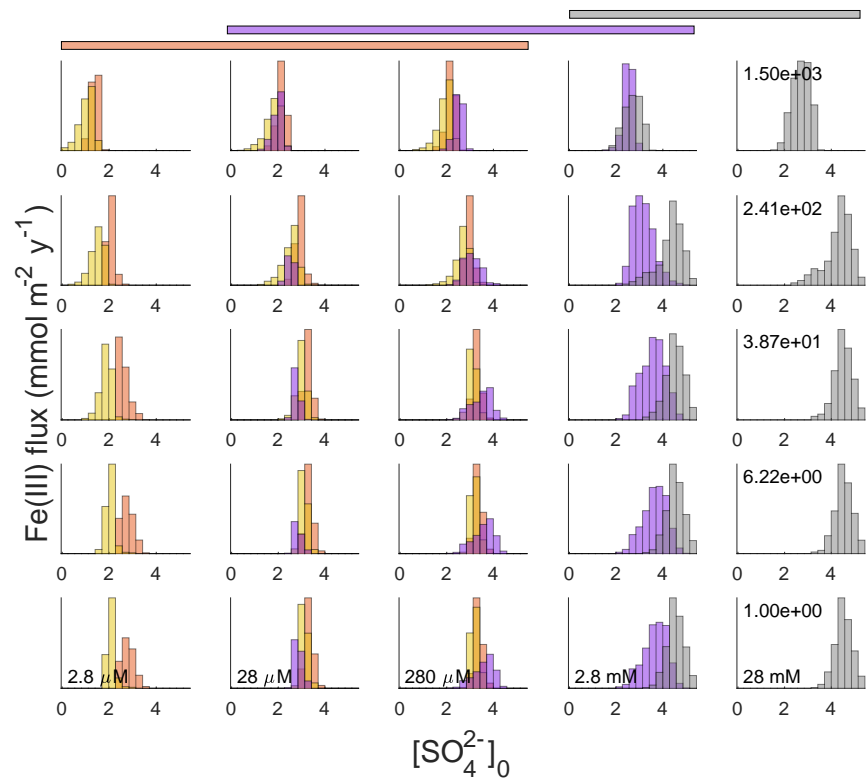


**Fig. S3.** Depth-integrated amount of hydrogen sulfide,  $\Sigma\text{H}_2\text{S}$ , on a logarithmic scale ( $\log_{10}$  of  $\text{mmol}/\text{m}^2$ ).

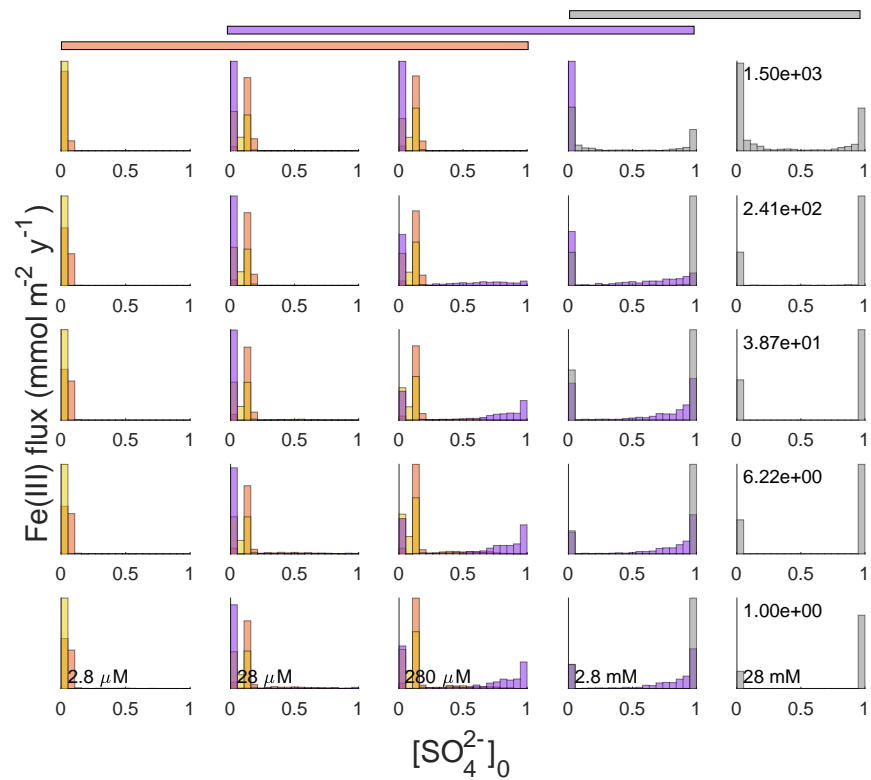


**Fig. S4.** Fraction of the anoxic portion of the simulated water column that is euxinic (defined as sulfide concentrations exceeding ferrous higher concentrations),  $(\Delta z_{eux}/\Delta z_{anoi})$ .

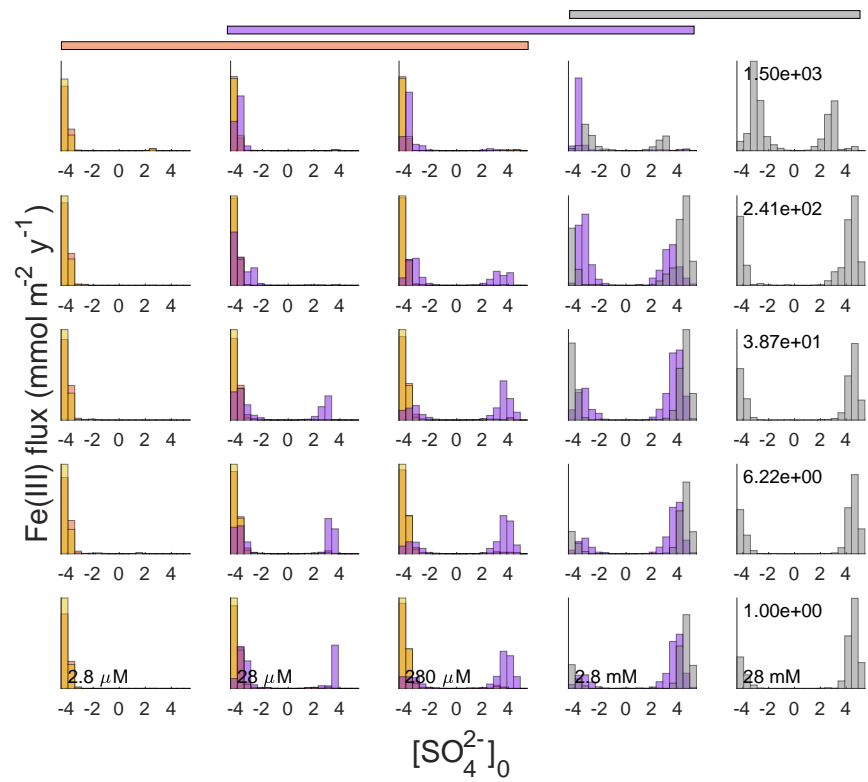


**Fig. S5.** Depth-integrated difference between the concentrations of total aqueous sulfide and dissolved iron ( $\Sigma([\text{H}_2\text{S}]_{tot} - [\text{Fe}^{2+}])$ ) ( $\log_{10}$  of  $\text{mmol m}^{-2}$ ). Values smaller than zero indicate predominantly ferruginous conditions.

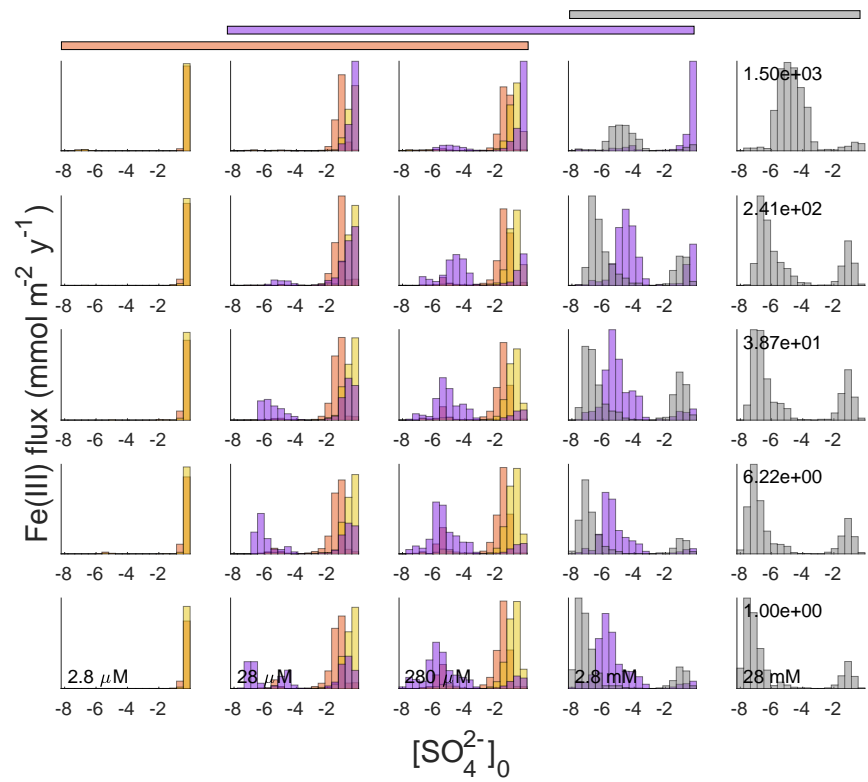


**Fig. S6.** Proportion of iron reduction in the total anaerobic mineralization of organic carbon in the water column,  $\Sigma R_{IR} / \Sigma (R_{IR} + R_{SR} + R_{CH_4})$ , on a logarithmic scale.

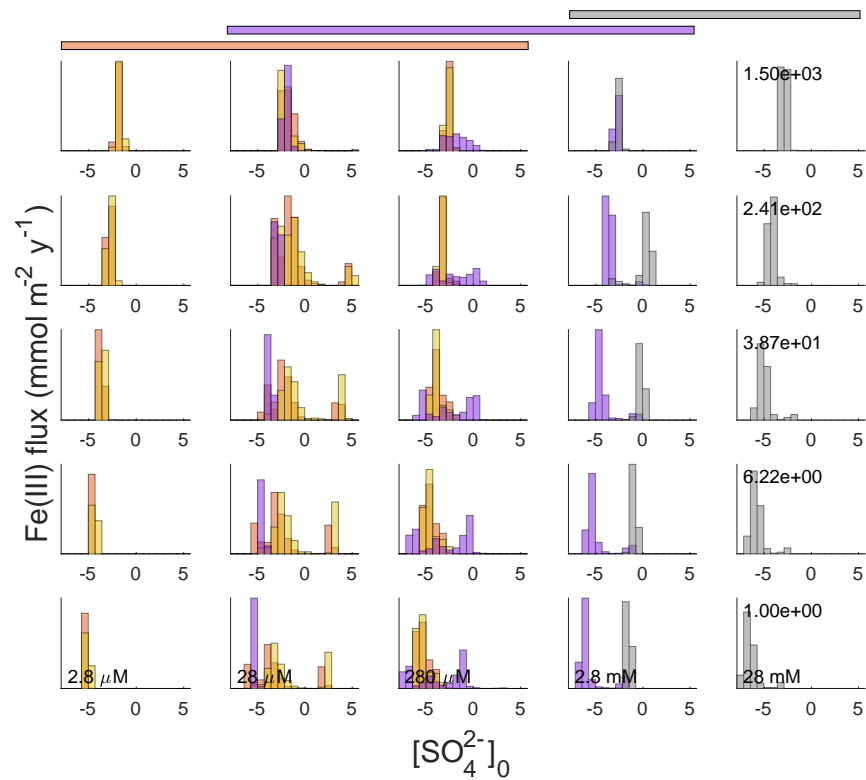


**Fig. S7.** Ratio of the depth-integrated rate of Fe-dependent AOM to the depth-integrated rate of S-dependent AOM ( $R_{Fe-AOM} : R_{S-AOM}$ ), on a logarithmic scale. Values smaller than zero indicate dominance of sulfate-dependent anaerobic oxidation of methane in the water column.

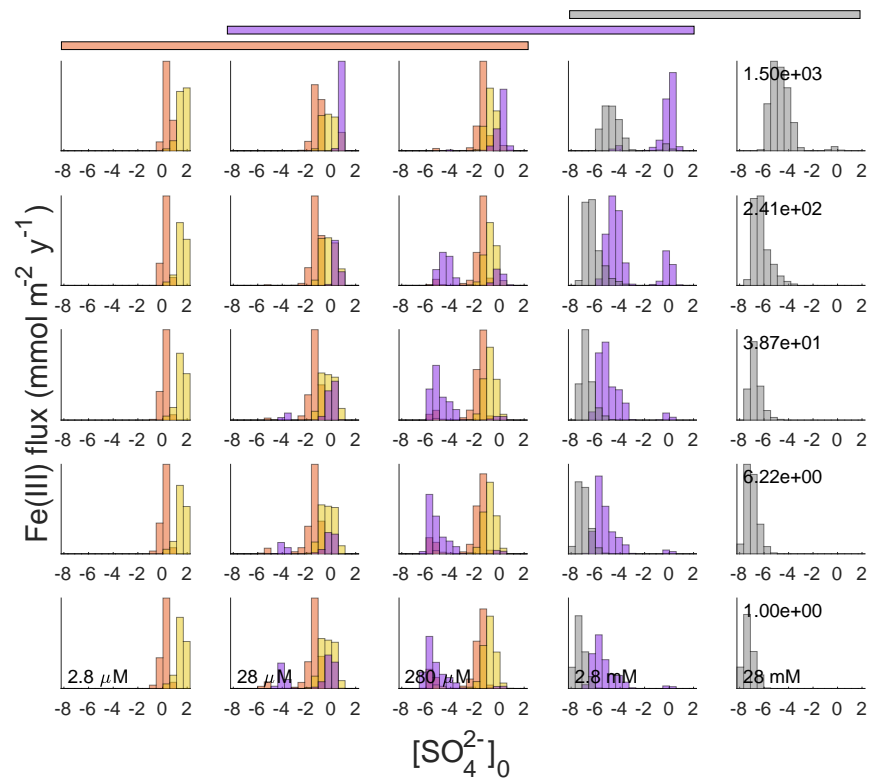


**Fig. S8.** Ratio of the depth-integrated rates of microbial iron reduction and microbial sulfate reduction ( $R_{IR} : R_{SR}$ ), on a logarithmic scale. Values greater than zero indicate dominance of iron reducers. Values smaller than zero indicate dominance of sulfate reducers.

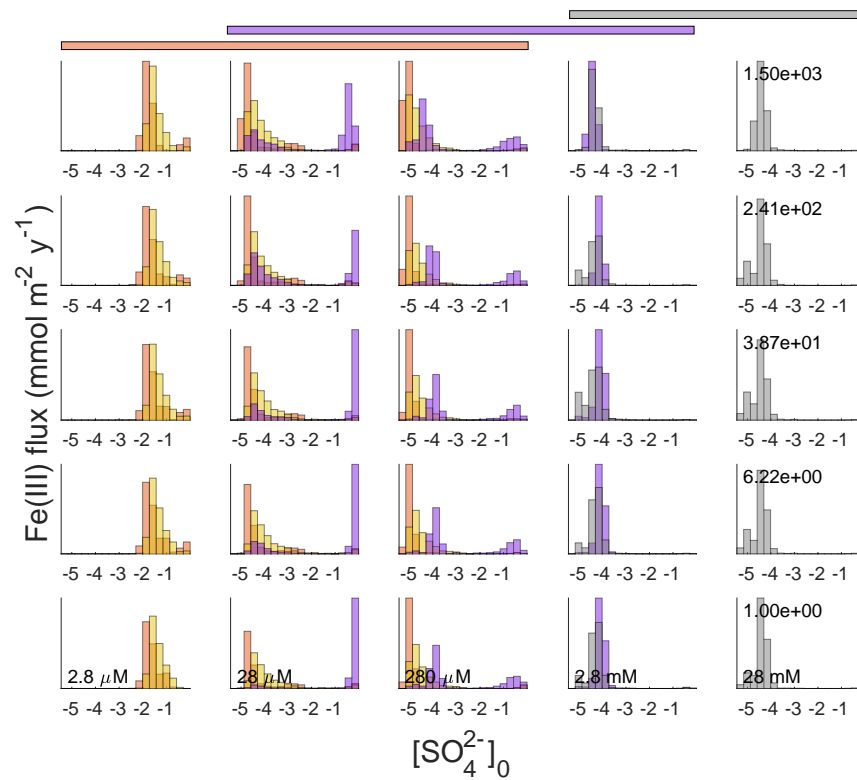


**Fig. S9.** Proportion of methanogenesis in the total anaerobic mineralization of organic carbon in the water column,  $\Sigma R_{CH_4} / \Sigma (R_{IR} + R_{SR} + R_{CH_4})$ , on a logarithmic scale.

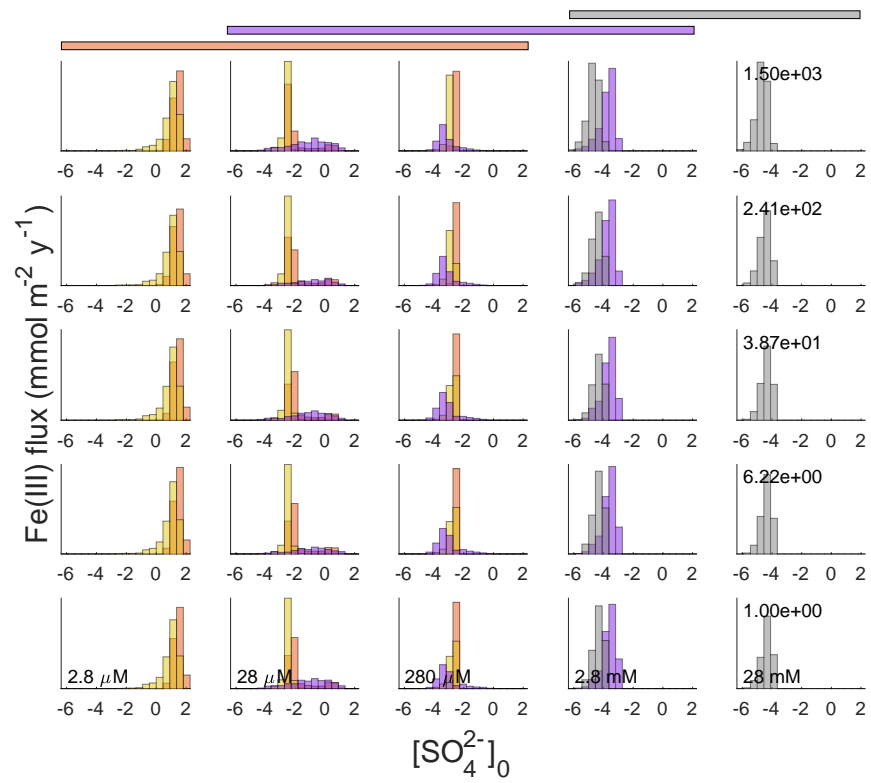


**Fig. S10.** Model-calculated flux of methane from water column towards the atmosphere ( $\log_{10}$  of  $\text{mmol}/\text{m}^2/\text{y}$ ).

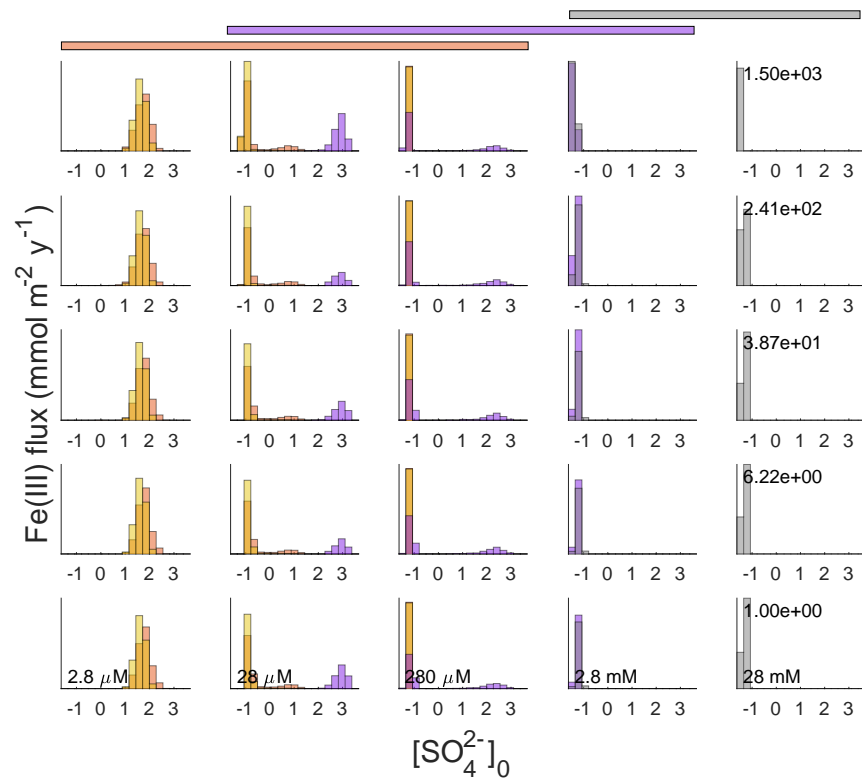


**Fig. S11.** Depth-integrated rate of methanogenesis in the water column,  $\Sigma R_{CH_4}$  ( $\log_{10}$  of mmol/m<sup>2</sup>/y).